High-Fidelity Electron Spin Gates for Scaling Diamond Quantum Registers

T. Joas,[1,*] F. Ferlemann,[2,5] R. Sailer,[1] P. J. Vetter,[1] J. Zhang,[1] R. S. Said,[1] T. Teraji,[3] S. Onoda,[4] T. Calarco,[2,5,6] G. Genov,[1] M. M. Müller,[2] and F. Jelezko[1,7]

[1]*Institute for Quantum Optics, Ulm University, 89081 Ulm, Germany*
[2]*Peter Grünberg Institute-Quantum Control (PGI-8), Forschungszentrum Jülich GmbH, 52428 Jülich, Germany*
[3]*Research Center for Electronic and Optical Materials, National Institute for Materials Science, Tsukuba, Ibaraki 305-0044, Japan*
[4]*Takasaki Advanced Radiation Research Institute, National Institutes for Quantum Science and Technology (QST), Takasaki, Gunma 370-1292, Japan*
[5]*Institute for Theoretical Physics, University of Cologne, 50937 Köln, Germany*
[6]*Dipartimento di Fisica e Astronomia, Universitá di Bologna, 40127 Bologna, Italy*
[7]*Center for Integrated Quantum Science and Technology (IQST), Ulm University, 89081 Ulm, Germany*

(Received 16 August 2024; revised 25 November 2024; accepted 18 February 2025; published 27 May 2025)

Diamond is a promising platform for quantum information processing as it can host highly coherent qubits that could allow for the construction of large quantum registers. A prerequisite for such devices is a coherent interaction between nitrogen-vacancy (NV) electron spins enabling scalable entanglement. Entanglement between dipolar-coupled NV spin pairs has been demonstrated but with a limited fidelity, and its error sources have not been characterized. Here, we design and implement a robust two-qubit gate between NV electron spins in diamond and quantify the influence of multiple error sources on the gate performance. Experimentally, we demonstrate a record gate fidelity of $F_{2\mathrm{q}} = (96.0 \pm 2.5)\%$ under ambient conditions. Our identification of the dominant errors paves the way towards NV-NV gates beyond the error correction threshold.

DOI: 10.1103/PhysRevX.15.021069 Subject Areas: Quantum Physics

I. INTRODUCTION

Quantum processors have evolved from a scientifically intriguing concept into powerful devices on the verge of solving certain computational problems efficiently [1–3]. Their success has been enabled by the increased number of controllable qubits on recent devices, which can reach three-digit numbers [3,4]. Nevertheless, many compelling computational problems require operating quantum error correction protocols on thousands of individually controllable qubits, connected through high-fidelity multiqubit gates. Each quantum platform faces technical challenges in scaling towards this goal [5–8]. Actual devices supporting error correction have only modest size [9–12], or they have not been tasked with computational problems yet [4].

Nuclear spin qubits in diamond, which are controlled by a single nitrogen-vacancy (NV) electron spin, offer gate fidelities among the leading platforms [13,14], reaching 99.94% [15] and 99.93% [15] for single-qubit and two-qubit gates, respectively, and support register sizes of up to ten nuclear spins [16,17]. Their capability to operate under ambient conditions can lower requirements on experimental infrastructure and classical control electronics, potentially allowing preservation of high-fidelity gates as the number of qubits increases. However, scaling up the register size in diamond with a single NV is restricted by the limited range of the nuclear dipolar interaction and spectral crowding, making diamond a challenging candidate for building quantum processors capable of error correction.

To overcome these scaling limitations, photon-mediated entangling gates [18] have been implemented as a proof of concept to optically link separate nuclear registers [19,20], albeit with low entanglement rates. Complementarily, it is appealing to directly connect multiple nuclear spin registers within the same diamond by coupling their central NV spins via the longer-range electron dipolar interaction. A central capability for such a connection, electron spin entanglement, has already been achieved but with a limited fidelity [21–23]. Improved performance is possible for state-to-state transfers in NV-NV registers with optimal control microwave pulses [24]. However, optimization of a full two-qubit gate for arbitrary input states remains a

[*]Contqct author: timo.joas@alumni.uni-ulm.de

Published by the American Physical Society under the terms of the Creative Commons Attribution 4.0 International license. Further distribution of this work must maintain attribution to the author(s) and the published article's title, journal citation, and DOI.

significant challenge at room temperature as the available error metrics imply increased measurement time and higher computational overhead [15,25,26]. Furthermore, experimental implementation is often impeded by the individual, nonlinear microwave response of each experimental setup.

In this work, we apply an alternative approach to optimal control for fidelity improvement, where we characterize the physical error sources. Starting with a relatively simple gate, we analyze how errors affect its dynamics via a combination of experiments and simulations. Modeling the physics of the full system of four spins (two electron spins plus two nuclear spins) enables us to quantify gate error sources that determine the entangling gate fidelity and to mitigate their effect in a targeted manner. Thus, we can apply simple, sine-envelope [27,28] microwave pulses while optimizing the entangling gate parameters (see Sec. IV), which directly contribute to gate infidelity.

To demonstrate the effectiveness of our approach, we use randomized benchmarking to measure two-qubit gate fidelities in an electron spin quantum register in ambient conditions. We achieve a two-qubit gate fidelity of $F_{2\mathrm{q}} = (96.0 \pm 2.5)\%$, outperforming the reported Bell state fidelities in the literature [24]—even without the previously needed optimal control pulses.

As a result of the optimization, our gate operates close to the T_2 decoherence limit, and we characterize the remaining coherent errors. For diamond quantum computing hardware beyond the noisy intermediate-scale quantum era (NISQ [29]), the goal will be to surpass the error correction threshold. Our model projects that this objective is attainable at room temperature, and it identifies the physical mechanisms that promise the largest enhancements in fidelity. The prolonged electron coherence time (up to $T_2 \sim 1$ s [30]) at cryogenic temperature could further improve NV-NV gate fidelity.

II. RESULTS AND DISCUSSION

A. Diamond quantum register

The quantum register for our gate is fabricated by implanting $C_5N_4H_n$ molecules from an adenine ion source [31] into a ^{12}C enriched, epitaxially grown diamond layer [see Fig. 1(a) and details in Sec. IV]. Two of the four nitrogen atoms in the molecule can end up in close proximity (approximately 9 ± 4 nm) in the diamond lattice and form two negatively charged NV centers. The estimated probability of finding an NV pair in a confocal spot is about 15%. NV$^-$ initialization and readout are achieved optically: We initialize the spin state with a green laser pulse. If required, the charge state is probed by a weak orange laser pulse exciting only the negative charge state of the NV center [32]. Note that the NV centers are too close to be optically resolvable based on their spatial separation. Hence, room temperature, state-of-the-art readout allows one only to monitor the total fluorescence from both qubits upon green laser illumination. The readout signal is proportional to the summed qubit populations, but it lacks information about correlations between them (see Sec. IV) [21]. Each NV in the pair has a different orientation in the crystal lattice, resulting in spin sublevels of different energies when we apply a magnetic bias field, e.g., $|B| \sim 100$ G (Appendix A), of appropriate orientation. A continuous-wave optically detected magnetic resonance (ODMR) experiment thus shows four lines: two below and two above the zero-field splitting (ZFS) energy [Fig. 1(b)]. We define our qubit subspace by the choice of microwave transitions shown in the inset of Fig. 1(b). The difference in transition frequencies allows for single-qubit rotations by applying pulses with frequencies that match the resonance of the respective qubit.

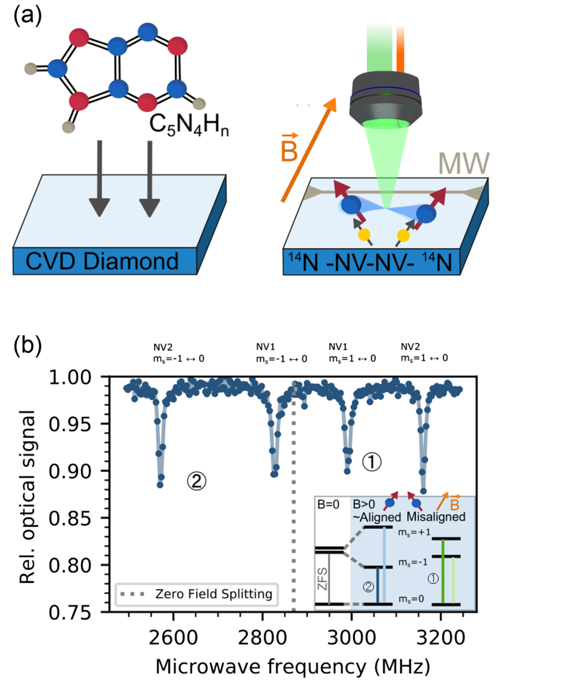

FIG. 1. Diamond quantum register. (a) Left: register fabricated by implanting adenine molecules into an epitaxially grown diamond layer. Right: coupled NV system (consisting of two NV centers plus their inherent ^{14}N nuclear spins) accessed optically with a confocal microscope. Spin states under a bias magnetic field $\vec{B}$ are manipulated through a microwave antenna. (b) Optically detected magnetic resonance spectrum of the register in panel (a). We employ the marked transitions 1 and 2 as "target qubit" and "control qubit." In principle, these labels are interchangeable. Inset: sketched energy diagram of a single NV without and with (blue background) magnetic field applied. Here, the control qubit is better aligned with the magnetic field and thus shows a higher splitting in the microwave domain.

We can detect the presence of a magnetic dipolar interaction of $v_{\mathrm{dip}} \sim 0.1$ MHz between NVs with a double electron-electron resonance [33] (DEER) experiment. As the coupling is smaller than the reciprocal dephasing time $1/T_2^* \sim 0.5$ MHz, the entangling gate needs to be

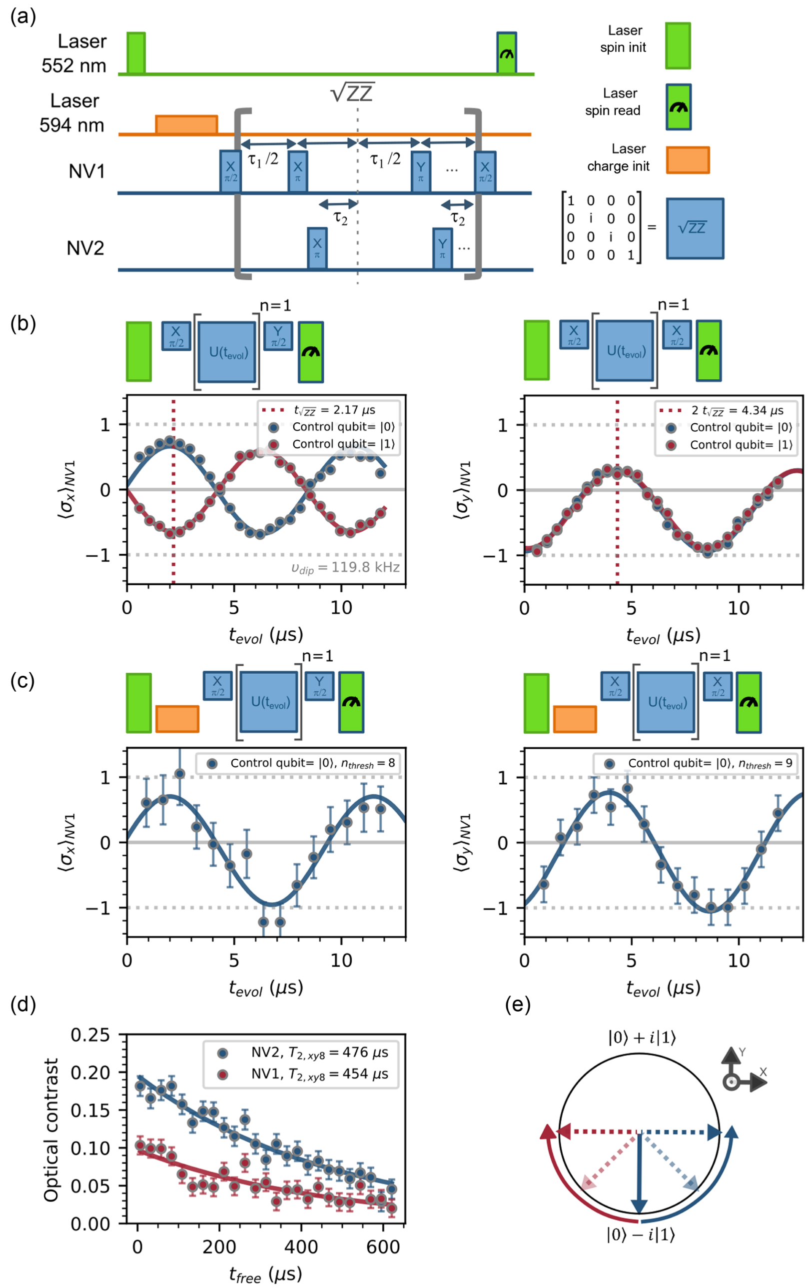

FIG. 2. Entangling gate. (a) Microwave and laser sequence for probing the $\sqrt{ZZ}$ entangling gate. Shown in blue are the envelope-shaped microwave pulses resonant with NV1 (target qubit) and NV2 (control qubit) of the labeled phase (X or Y) and pulse area ($\pi/2$ or π). For each NV, $N_\pi = 8$ (phase cycled with XY8-1) π pulses inside the gray brackets form the $\sqrt{ZZ}$ gate. For the sake of a clear figure, only two of the eight pulses per NV are drawn. The $\pi/2$ pulses around the gate are used to initialize the target qubit to the Bloch sphere equator and map the evolution under the gate onto the σ_z readout axis. In green, we show the 3 μs pulses of the 552-nm laser used for spin initialization and readout (blue stroke). Shown in orange are the 3.5-ms pulses of the 594-nm laser for optional charge-state initialization. The unitary matrix on the right is realized for a calibrated $\tau_1 = 800$ ns, $\tau_2 = t_{\sqrt{ZZ}}/N_\pi$, $n = 1$. (b),(c) Measured evolution of the σ_x, σ_y component of the target qubit for varying τ_2 in the $\sqrt{ZZ}$ gate sequence ($t_{\mathrm{evol}} = N_\pi n \tau_2$, here $\tau_1 = 3000$ ns, $n = 1$, $N_\pi = 8$; fitted with $y = A_s \sin(2\pi v_{\mathrm{dip}} + \phi_s) + y_{0,s}$, where $A_s, \phi_s, y_{0,s}$ are free parameters). The $\sqrt{ZZ}$ gate is realized after $t_{\sqrt{ZZ}}$. The target qubit is initialized and mapped onto σ_z as given by the respective microwave sequence. Charge initialization with threshold parameter $n_{\mathrm{thresh}} = 8, 9$ is applied for panel (c). (d) T_2 coherence measurements for both NVs by applying a XY8-n sequence with fixed pulse spacing $\tau_1 = 800$ ns sequence and varying order n_{xy} (total sequence duration $t_{\mathrm{free}} = 8 n_{\mathrm{xy}} \tau_1$) to only one of the NVs, respectively. Fixing τ_1 while increasing n_{xy} naturally compares to repeated application of our gate sequence that uses fixed τ_1, τ_2. (e) Idealized spin dynamic under the gate with an initial $\pi/2$ pulse as in panels (b) and (c) on the Bloch sphere equator of the target qubit for the case of control qubit state $= |0\rangle/|1\rangle$ (blue/ red). A control qubit conditioned rotation from $\tau_2 = 0$ with no acquired phase evolves for $\tau_2 > 0$.

embedded in a decoherence-protecting dynamical decoupling pulse sequence. Extending upon previous work [21] to increase the coherence during the operation, we employ a two-qubit gate that applies robust XY8 microwave pulse sequences [34] on both NVs [see Fig. 2(a)]. Tuning the spin-flip time τ_2 between the center of the π pulses on the second NV and the times when the first NV is refocused, we partially refocus the dipolar interaction, adjusting the effective interaction time and acquired phase. Equipped with single-qubit rotations and an entangling operation, we have a gate set that, in principle, allows for arbitrary two-qubit quantum computations [35].

B. Entangling gate

Our entangling gate, labeled the $\sqrt{ZZ}$ gate, is

$$U_{\sqrt{ZZ}} = \mathrm{diag}(1, i, i, 1) \tag{1}$$

in the basis of the computational basis states $\{|00\rangle, |01\rangle, |10\rangle, |11\rangle\}$ and up to a global phase (see Appendix D). We obtain additional intuitive understanding from the spin evolution on the Bloch sphere. To this end, we bring the first NV ("target qubit") into a superposition state and apply our $\sqrt{ZZ}$ gate sequence. Choosing such an input state renders the experiment a dynamically decoupled DEER [36], and varying the spin-flip time τ_2 allows us to measure the dipolar coupling (see Fig. 2).

In the σ_x component, we observe [Fig. 2(b)] that a sinusoidal evolution arises as more phase is acquired through the dipolar interaction by a longer τ_2 [sketch in Fig. 2(e)]. The controlled nature of the gate that is required for a computationally complete gate set is revealed by the reversed direction of the σ_x DEER oscillation when the control qubit is initialized into $|1\rangle$. We extract the dipolar coupling $v_{\mathrm{dip}} = (119.8 \pm 1.0)$ kHz between the two NVs from the fitted sine oscillation frequency. Thus, we find a calibrated evolution time $t_{\sqrt{ZZ}} = N_\pi \tau_{2,\sqrt{ZZ}} = (2.17 \pm 0.02)$ μs and describe details and optimization of the π pulse spacing $\tau_1 = 800$ ns in Appendix D. When calibrating, we minimize unwanted interactions with the inherent ^{14}N nuclear spins [37] due to the misaligned magnetic field to the NV axes.

An important aspect of the gate performance is inferred from the sine oscillation amplitude and offset parameters (ideally, $A_s = 1$, $y_{0,s} = 0$). The apparent nonzero offset in Fig. 2(b) can be explained by the imperfect initialization of the NV charge state. If any of the NVs are neutrally charged (NV^0), no ZZ phase is collected during the $\sqrt{ZZ}$ gate; the output state is independent of τ_2 and thus far off the target state. Applying a green (552-nm) laser pulse yields a steady-state charge distribution of around 0.7 NV^- and 0.3 NV^0 for a single NV [38] and thus a probability of $p(\mathrm{NV}^-, \mathrm{NV}^-) = 0.49$ for both NVs to be in the desired negative charge state. Overall, the observed oscillation is an average over the different charge cases, which lowers the contrast of the σ_x, σ_y oscillation in Fig. 2(b). Second, the σ_y component becomes asymmetric (offset parameter of fitted sine $y_{0,s} < 0$), as this component is $\langle \sigma_y \rangle_{\mathrm{NV1}} = -1$ for all τ_2 given a wrong charge state and the degree of asymmetry $(|y_{0,s}|/A_s)$ can be a direct measure of the expected charge state of the NV pair (Appendix E).

In Fig. 2(c), we mitigate the charge initialization error by using a weak orange laser that employs thresholding (with a parameter n_{thresh}) over datasets containing all detected fluorescence photons [32]. The DEER oscillations in Fig. 2(c) show improvements in contrast and asymmetry of the σ_y component. However, there remains a significant deviation from full, symmetric contrast, which is in accordance with the limited charge-state fidelity $F_{\mathrm{NV-,NV-}} = (83 \pm 6)\%$ measured separately in Fig. 8. We also show that the charge-state fidelity can be improved by increasing the threshold parameter n_{thresh} of the post-selection. However, stricter thresholding comes at the cost of a worsened signal-to-noise ratio. Nevertheless, higher photon collection efficiency—provided, e.g., by micro-structured lenses [39], multilaser pulse excitation [40], or doping-induced NV charging [41–43]—could enhance charge-state fidelity significantly.

Given the minimal gate time $1/(2v_{\mathrm{dip}}) = 4.2$ μs and the coherence times $T_{2,\mathrm{XY8}} = (454 \pm 58)$ μs, (476 ± 30) μs for each NV measured in Fig. 2(d), we calculate a coherence limit for the entangling gate fidelity of 99.1%, and 98.6% for our exact microwave gate with the actual τ_1. However, our analysis in Sec. II E reveals that, in the long coherence regime enabled by dynamical decoupling, gate errors related to the ^{14}N nuclear spins become significant. We note that the slight asymmetry of the applied sequence on NV2 might not be optimal in terms of robustness [44], but such sequences have been demonstrated to be favorable for decoupling in the presence of crosstalk errors [45]. In addition, asymmetry allows us flexibility in terms of the choice of τ_1 and the total gate duration.

C. Repetitive benchmarking

Imperfections that are not related to the state evolution during a gate are commonly referred to as state preparation and measurement errors (SPAM) [46].

We use repetitive benchmarking, i.e., repeated application of the gate to a certain input state [47], to separate the entangling gate fidelity from SPAM errors. We demonstrate that this tool quantifies gate errors independently of the charge state. The latter error can be significantly reduced by charge-state mitigation strategies, as described in the previous section.

Separation of the gate error is achieved by repeated application of the gate under test. After n repetitions, single-qubit rotations are applied to map back to the ground state, and the $\langle \sigma_z \rangle$ expectation value is measured.

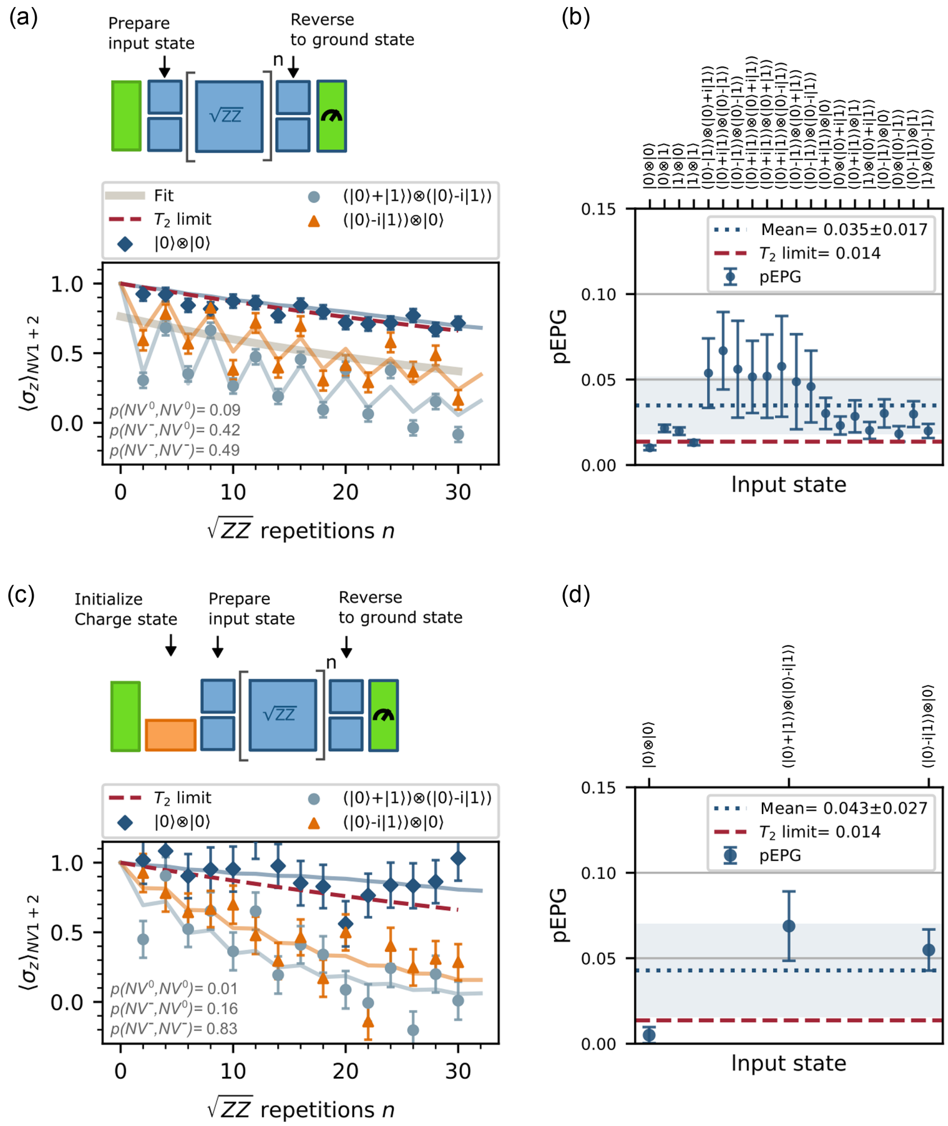

FIG. 3. Repetitive benchmarking. (a),(c) Measured surviving population after n applications of the $\sqrt{ZZ}$ gate. For each data point, a reverse circuit is added that returns to $|00\rangle$ in the absence of gate and preparation errors. Data are shown for exemplary input states, an exponential fit (gray line) to extract the pEPG for input state $(|0\rangle - i|1\rangle) \otimes |0\rangle$ (simplifying notation, this abbreviates $|\Psi\rangle_{\mathrm{NV1}}|\Psi\rangle_{\mathrm{NV2}} = (|0\rangle - i|1\rangle)/\sqrt{2} \otimes |0\rangle$ with dropped normalization throughout this work), and simulation results including the charge-state behavior (colored solid lines, charge-state probabilities annotated). (b),(d) Extracted pEPG from the data in panels (a) and (c) for all probed input states. The charge-state-induced modulation in the decay data described in the main text leads to the plotted 1σ fit errors that depend on the input state. Blue shading represents the standard deviation of all data points. Charge initialization is applied for panels (c) and (d). The mean is calculated as an average over the mean pEPGs of each input state group to ensure comparability between panels (b) and (d).

In the resulting decay curves, errors occurring during the gate operation are collected in the lifetime parameter of a fitted model, which we convert to a pseudo error per gate (pEPG) metric (see Sec. IV).

Figure 3(a) shows decays for repeated $\sqrt{ZZ}$ gates for three input states. We find a mean $\overline{\mathrm{pEPG}} = 0.035 \pm 0.017$ averaged over all tested input states [see Fig. 3(b)], corresponding to a pseudo gate fidelity of $\mathrm{p}F_{2\mathrm{q}} = 1 - \overline{\mathrm{pEPG}} = (96.5 \pm 1.7)\%$. This is only a factor of 2.5 away from the T_2 limit $\mathrm{pEPG}_{T2} = 0.014$ that we calculate from an independent coherence measurement [Fig. 2(b)]. Thus, coherent gate errors are qualitatively small, and later, we will quantify the different contributions.

The input states can be grouped into three classes of pEPGs: The computational basis states show the lowest gate errors due to their magnetic noise insusceptibility. Gate errors increase when one qubit is in a superposition input state because of decoherence during the gate operation. Finally, input states with both qubits in superposition yield entangled states for gate repetitions n with $\mathrm{mod}(n, 2) = 1$. Thus, not only will both qubits be affected by decoherence, but some entangled states will also pick up this noise more efficiently [48].

A prominent feature in repetitive benchmarking is an additional modulation with a period of $n = 4$ for input states that are not the computational basis states. This behavior is a consequence of the charge-state SPAM error. When one of the NVs is initialized as NV^0, the coupling is $\nu_{\mathrm{dip}} = 0$. This SPAM error has no effect when the initial state is a computational basis state. However, imperfect initialization reduces the output-state fidelity when any of the NVs are in a superposition state, with double superposition states showing the greatest error [see Fig. 3(a)]. We simulate the repetitive benchmarking experiment in Figs. 3(a) and 3(c) considering all charge-state configurations (see details in Sec. IV). The experimentally observed dependence of the modulation depth on the chosen input state is well reproduced.

When adding charge-state initialization to the repetitive benchmarking in Fig. 3(c), the modulation is reduced, and we extract a slightly elevated $\overline{\mathrm{pEPG}} = 0.043 \pm 0.027$. Comparing this mean $\overline{\mathrm{pEPG}}$ for the charge-initialized case in Fig. 3(d) with the steady-state initialized data in Fig. 3(b), we find agreement within the standard deviation calculated from the data of all input states.

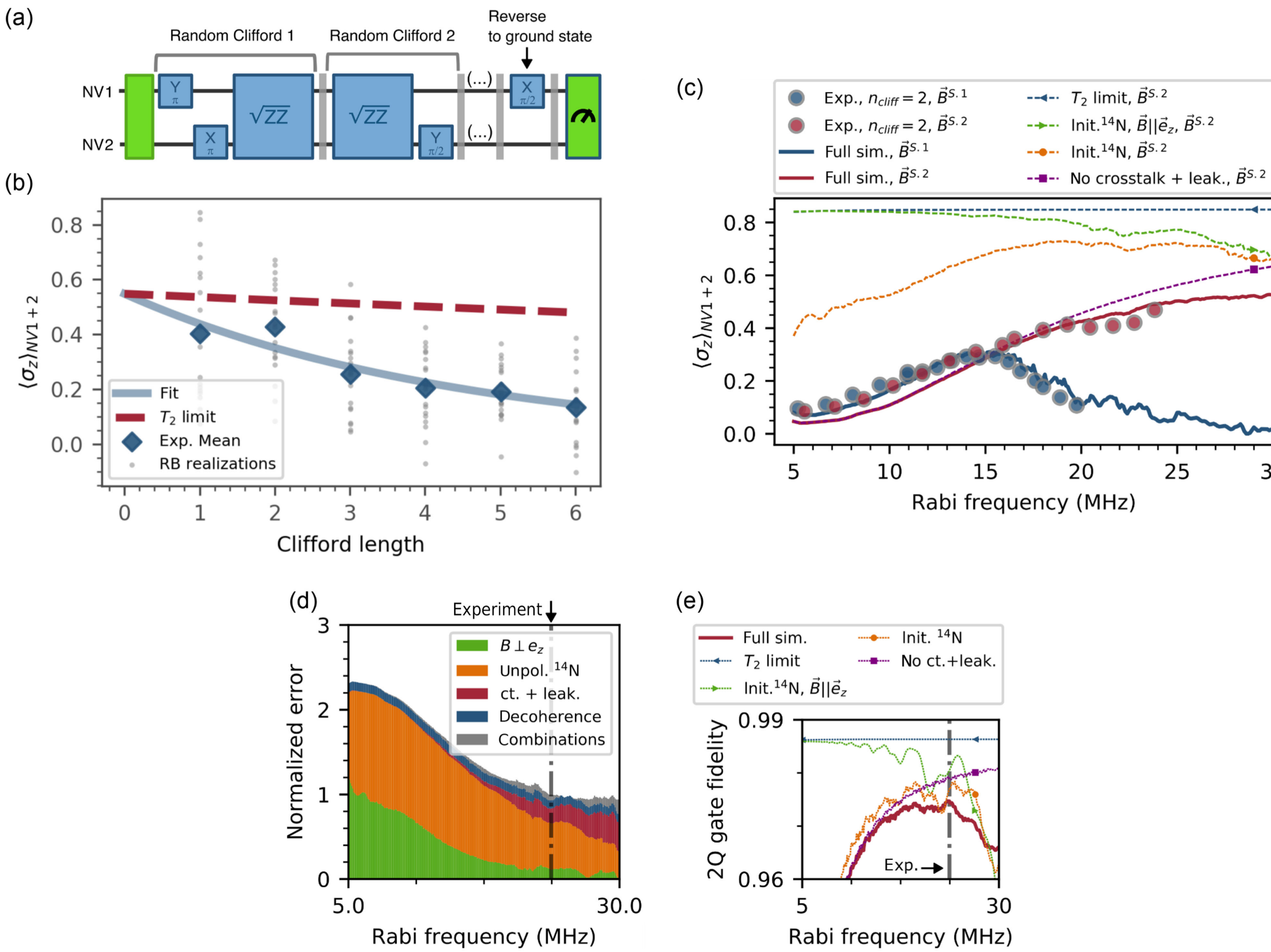

FIG. 4. Randomized benchmarking and gate error analysis. (a) Sketched gate sequence for a single randomized benchmarking data point. Random Clifford gates are generated and reversed to the ground state. (b) Surviving population after randomized benchmarking in our optimized experimental setting [magnetic field setting 2, $\Omega_{\mathrm{Rabi}}/(2\pi) = 23.7$ MHz, 20 random experiments per Clifford length]. From a single-exponential fit, the EPC of the gate set discussed in the main text is extracted. (c) Randomized benchmarking at a fixed Clifford length $n_{\mathrm{Cliff}} = 2$ for varying Rabi frequencies ($\Omega_{\mathrm{Rabi}} = (\pi/t_\pi)$ with approximately the same duration t_π of sine envelope-shaped π pulses for both NVs). Each data point is a mean of 20 random experiments. The solid blue (red) line is a simulation at magnetic field setting 1, about 60 G (magnetic field setting 2, about 100 G), which contains a free parameter to account for the experimental SPAM errors (see Sec. IV). From the dashed lines, which are simulations at magnetic field 2 where the labeled error sources—i.e., crosstalk plus leakage, unpolarized ^{14}N spin, magnetic field orthogonal to the orientations of the NVs e_z—are turned off, we extract the relative error contributions in panel (d). (d) Error contributions to the gate set for varying Rabi frequencies, normalized to the error at the experimental $\Omega_{\mathrm{Rabi}}/(2\pi) = 23.7$ MHz, magnetic field 2. The attribution to the labeled error sources is presented in Sec. IV. (e) Simulated gate fidelity of the $\sqrt{ZZ}$ gate. The dashed lines selectively disable error sources as in panel (c), with only decoherence left for the blue dashed line.

D. Randomized benchmarking

Randomized benchmarking [46] has emerged as a standard tool to evaluate gate performance, yielding a fidelity metric of an average computation with *a priori* limited insight into the nature of the gate error. In contrast to repetitive benchmarking, this fidelity can be directly compared to values obtained on different quantum hardware platforms [49–51]. We perform two-qubit randomized benchmarking in Figs. 4(a) and 4(b) (details in Sec. IV).

In our optimized setting [magnetic field 2 in Table I unless stated otherwise, $\Omega_{\mathrm{Rabi}}/(2\pi) = 23.7$ MHz], we achieve an entangling gate fidelity of $F_{2\mathrm{q}} = (96.0 \pm 2.5)\%$ as extracted from an error per two-qubit Clifford gate $\mathrm{EPC} = (14.9 \pm 2.7)\%$ and precharacterized average effective single-qubit errors of $F_{1\mathrm{q}} = (99.23 \pm 0.12)\%$ [see Eq. (9), Appendix C]. Our entangling gate fidelity is better than the best-reported NV-NV entangled state fidelity (82.4% [24]) that was optimized by state-to-state transfer optimal control algorithms. We emphasize that the improved performance takes into account errors for arbitrary input states, in contrast to a state-to-state transfer fidelity. As we perform no charge-state initialization, the measured SPAM error, represented in the amplitude parameter of the fitted exponential decay, is non-negligible. The decay's lifetime is substantially shorter than the decoherence limit ($\mathrm{EPC}/\mathrm{EPC}_{T2} = 5.9 \pm 1.1$). We attribute this feature to other, coherent errors.

E. Gate error sources

Three error sources (explained in detail in Appendix G) mainly limit our gate set fidelity: the unpolarized ^{14}N nitrogen spins, the misaligned magnetic field, and microwave crosstalk and leakage. We measure their influence by performing two-qubit randomized benchmarking while varying the Rabi frequency of all pulses of the gate set. To keep the measurement time viable, we determine only the surviving population $\langle\sigma_z\rangle_{\mathrm{NV1+2}}$ for a fixed Clifford length $n_{\mathrm{cliff}} = 2$. This approach allows us to extract relative error contributions, as described in Sec. IV, but yields no absolute gate error metric [25]. Increasing the Rabi frequency drives the hyperfine lines due to the ^{14}N spin more homogenously, but it is only beneficial until microwave crosstalk and leakage become limiting. For our magnetic field setting 1 [blue line in Fig. 4(c), exact parameters in Table I] with modest frequency separation, the optimal

TABLE I. Parameters as chosen and estimated in the simulation. The computational basis of the qubit system (defined as $|0\rangle = |g\rangle, |1\rangle = |e_{1/2}\rangle$) employs the new spin eigenstates (due to the tilted quantization axis) that are superpositions of the $m_s = |0\rangle, \pm|1\rangle$ electron spin states, with $|g\rangle$ referring to the spin ground state and $|e_{1/2}\rangle$ to the excited spin eigenstates (lower or higher transition frequency than ZFS).

Magnetic field setting	Setting 1 $\lvert\vec{B}^{\mathrm{S.1}}\rvert \sim 60$ G		Setting 2 $\lvert\vec{B}^{\mathrm{S.2}}\rvert \sim 100$ G	
NV center (gate sequence/physical order)	NV1/NVA	NV2/NVB	NV2/NVA	NV1/NVB
Zero-field splitting and axial strain $D/(2\pi)$	2865.42 MHz	2867.27 MHz	2865.42 MHz	2867.27 MHz
Transversal strain $E/(2\pi)$	0 MHz			
Transition frequencies f_i	2932.5 MHz	2751.8 MHz	2571.0 MHz	2990.8 MHz
(*): unused	2829.4 MHz (*)	2999.4 MHz (*)	3160.2 MHz (*)	2827.3 MHz (*)
Frequency separation $\mathrm{Min}(\lvert f_i - f_j\rvert)$	66.9 MHz		163.5 MHz	
Absolute magnetic field $\lvert B\rvert$	64.23 G	63.10 G	105.33 G	
Absolute magnetic field (electron/nuclear) $\lvert\omega_{\mathrm{e},i}\rvert/(2\pi) = \gamma_{\mathrm{e}}\lvert B\rvert/(2\pi)$ $\lvert\omega_{\mathrm{n},i}\rvert/(2\pi) = \gamma_{\mathrm{n}}\lvert B\rvert/(2\pi)$	180.01 MHz/19.76 kHz	176.85 MHz/19.42 kHz	295.18 MHz/32.41 kHz	
Misalignment θ_i	73.42°	45.53°	3.58°	74.08°
Quadrupole moment $Q/(2\pi)$	−4.945 MHz [52]			
^{14}N off-axis hyperfine coupling $A_{xx}/(2\pi) = A_{yy}/(2\pi)$	−2.62 MHz [53]			
^{14}N on-axis hyperfine coupling $A_{ZZ}/(2\pi)$	−2.162 MHz [52]			
Angle between NV centers β	70.53°			
Magnetic field orientation phi φ	47.94°		172.73°	
Effective dipole-dipole coupling strength $\nu_{\mathrm{dip}} = g/(2\pi)$	0.13995 MHz		0.11261 MHz	
Computational basis of qubit system $\lvert 0\rangle, \lvert 1\rangle$	$\lvert g\rangle, \lvert e_2\rangle$	$\lvert g\rangle, \lvert e_1\rangle$	$\lvert g\rangle, \lvert e_1\rangle$	$\lvert g\rangle, \lvert e_2\rangle$
Readout contrast α_i	14.6%	14.6%	19.4%	10.7%
Gyromagnetic ratio (electron/nuclear)				
$\gamma_{\mathrm{e}}/(2\pi)$	−28.02495 GHz/T [54]			
$\gamma_{\mathrm{n}}/(2\pi)$	3.076272 MHz/T [55]			

Rabi frequency is around $(2\pi)15$ MHz. Our optimized magnetic field setting 2 [red line in Fig. 4(c)] exhibits reduced gate errors due to a large frequency separation that mitigates microwave crosstalk and leakage. Simultaneously, these errors are minimized by employing pulse envelope shaping (here, sine envelope) for all microwave pulses [27,28].

However, at a higher magnetic field, state mixing for the misaligned NV1 becomes relevant. We estimate the SPAM error introduced solely by spin mixing at the higher magnetic field setting to around 17% by Rabi measurements on both spins in Fig. 9(a).

We employ a model (Sec. IV) that accurately describes the experimental randomized benchmarking results and quantifies the influence of different gate error sources. In Fig. 4(c), the experimental data at Clifford length $n_{\mathrm{Cliff}} = 2$ are well reproduced by our simulation for both magnetic field settings. Turning off one error source at a time, we can extract the relative error contributions to our gate set for our optimized setting in Fig. 4(d). At the experimentally chosen $\Omega_{\mathrm{Rabi}}/(2\pi) = 23.7$ MHz, the largest error contribution of 55% is due to the unpolarized ^{14}N spin. The misaligned magnetic field makes up for 11% of the observed error, with crosstalk and leakage contributing 17%, demonstrating the efficacy of our pulse envelope shaping. We note that each individual coherent error source investigated in Fig. 4 could, in principle, be corrected by adapting existing control techniques [56–58]. Their interplay and robustness within the complex four-spin Hamiltonian require further research. The relative decoherence contribution, estimated from $T_{2,\mathrm{XY8}} = 454$ μs and 476 μs per qubit, is 10%.

Finally, we project the achievable entangling gate fidelity directly from our model under a realistic scenario for future experiments in Fig. 4(e) (97.5% simulated at our experimental settings, including decoherence). Addressing all discussed coherent errors would place our gate fidelity at the coherence limit of 98.6%. Two-qubit gate fidelities of 99.6% that support realistic error correction protocols [59,60] are achievable by additionally extending the coherence time of the register by higher-order dynamical decoupling (see Sec. IV).

III. CONCLUSION AND OUTLOOK

We have experimentally demonstrated the highest entangling gate fidelity of $F_{2q} = (96.0 \pm 2.5)\%$ between solid-state electron spins at room temperature. Our analysis of the gate error sources reveals that 90% of those errors are coherent and correctable.

The primary gate error sources are the unpolarized nitrogen spin, which could be addressed by adapting one of the existing nitrogen-spin polarization techniques [61–64] to our magnetic field regime, and the misaligned magnetic field, which is unavoidable for NV geometries with different orientation in the crystal lattice. A perfectly aligned magnetic field would be possible for NV quantum registers of the same orientation that are conceivable when applying strong magnetic gradient fields [65,66] (around 1 G/nm) or leveraging different nitrogen isotopes of each NV, and it would allow a magnetic field strength compatible with straightforward nitrogen-spin polarization [63]. The smaller remaining microwave errors (crosstalk and leakage) could be mitigated by optimal control [57,67–69].

We found that we incur a non-negligible SPAM error due to spin mixing in the misaligned magnetic field. Operating at cryogenic temperatures (around 4 K) would significantly decrease both of the current initialization errors. First, resonant laser excitation of the sharp optical absorption lines [70] would enable fast, high-fidelity charge-state initialization [71,72]. Additionally, spin mixing errors could be avoided for arbitrary magnetic field geometries, as spin initialization would be possible without cycling through the NV singlet state [71] and thus would be independent of the off-axis magnetic field component. Furthermore, operating at low temperatures of around 4 K improves coherence times by several orders of magnitude, up to seconds [30], effectively mitigating the detrimental effect of decoherence on gate fidelities. Last, narrow optical lines would allow us to distinguish the emitted photons spectrally, and combining with single-shot readout techniques [71,73] could enable us to measure spin correlations between the NVs.

Integrating up to four [74] coherently coupled NV centers each with nuclear spin registers of around 25 qubits [15–17] is possible with our current experimental technique. Our error analysis suggests that the gate fidelities on such a diamond quantum processor could support error-corrected operation of logical qubits. Efficient error suppression will additionally necessitate [9,12,75,76] fast, high-fidelity optical readout of nuclear [71,73] and electron spins [77,78].

IV. METHODS

A. Gate fidelity optimization

To obtain the experimental parameters realizing our highest gate fidelities, we utilize the following optimization strategy:

(1) $\hat{\vec{B}}$: We align the magnetic field orientation, such that it approximately yields equally spaced, microwave transition frequencies and thus reduced crosstalk and leakage. As a result, the field is closely aligned with one of the NV centers. This method also suppresses interactions with the nitrogen nuclear spin of this NV during the two-qubit gate, as the hyperfine tensor $\underline{A}$ remains diagonal.

We continue by iterative application of the following steps, each of which optimizes F_{2q} with respect to one of the remaining gate parameters:

(2) τ_1: The undesired interaction with the nitrogen spin is strongly pronounced on the more misaligned NV. In Appendix D, we show how to select a τ_1 that

minimizes this undesired interaction during the $\sqrt{ZZ}$ gate. However, $\tau_1 > 2\tau_2$ reduces the effective dipolar interaction during the gate operation, leading to increased decoherence.

(3) $|\vec{B}|$: We simulate the two-qubit gate fidelity and find the magnetic field strength that maximizes F_{2q}. Note the trade-off discussed in Appendix F: Higher $|\vec{B}|$ can increase gate fidelity, but it lowers the electron spin initialization fidelity. Our final setting $\vec{B}^{S.2}$ is found in Table I.

(4) Ω_{Rabi}: The same model is used to find the Rabi drive power that maximizes F_{2q} as in Fig. 4(e). We choose equal power for all microwave pulses in the gate set. Further improvement is possible by optimizing the power for all pulses independently [see Fig. 10(b)].

(5) τ_2: We experimentally calibrate the phase picked up by the dipolar interaction during the $\sqrt{ZZ}$ gate, which weakly depends on Ω_{Rabi}, as described in Appendix D.

B. Sample

The sample used in this study is a type-IIa (100) single-crystalline diamond film that is homoepitaxially grown on a high-pressure, high-temperature, type-Ib substrate via microwave-plasma-assisted CVD [79]. The CVD film thickness is 20 μm. To suppress the effects of ^{13}C on the coherence properties of the NV centers, a ^{12}C-enriched (99.95%) high-purity (nitrogen concentration less than 1 ppb) diamond is used. The ion implantation process of this sample was already described elsewhere [31]. Ionized $C_5N_4H_n$ ions are extracted from adenine powder and accelerated to 65 keV kinetic energy. The implantation fluence of $10^8\ \mathrm{cm}^{-2}$ is achieved after 10 s. After ion implantation, the sample is annealed at 1000 °C for 2 h in a forming gas (4% H_2 in Ar) to create NV centers and recover the diamond lattice. The sample is annealed in an oxygen environment at 465 °C for 4 h, followed by cleaning in a 1∶1∶1 mixture of HNO_3, H_2SO_4, and $HClO_4$ at 200 °C under a pressure of 6–8 bar for 30 min.

For the NV pair used as a quantum register, we measure dephasing (Ramsey) and decoherence (Hahn echo, XY8) times of $T_2^* = (2.60 \pm 0.11)$ μs; (2.37 ± 0.13) μs, $T_{2,\mathrm{HE}} = (55 \pm 11)$ μs; (150 ± 9) μs, $T_{2,\mathrm{XY8}} = (454 \pm 58)$ μs; and (476 ± 30) μs on NV1 and NV2, respectively. Our pulse spacing definition of type $(\pi/2) - (\tau/2) - \pi - (\tau/2) - (\pi/2)$ with pulse spacing τ for the Hahn echo differs by a factor of 2 from Ref. [80], making it comparable with higher-order decoupling sequences. Based on our prior work [31], we estimate the creation yield of NV pairs with similar coherence to approximately 1.7%. The ratio of NV pairs to single NVs in the sample is approximately 1 : 6.5.

C. Setup

We control and read the NV's spin and charge state with a standard home-built confocal microscope. Spin initialization and readout laser pulses of 3000 ns at a wavelength of 552 nm (green) are generated by a cw laser and an acousto-optic modulator (AOM). The orange (594-nm) charge initialization pulses from a different, digitally modulated cw laser are 3.5 ms long and of circular polarization to ensure equal ionization rates for both NVs during the charge initialization. The polarization of the green laser is linear and adjusted for nearly equal readout contrast for data in Fig. 3. For Figs. 2 and 4, the chosen polarization realized contrasts as listed in Table I.

All laser pulse shapes and microwave waveforms are sampled on an arbitrary wave generator (Keysight M8195A) amplified and applied to the NV through a copper wire of 20 μm diameter placed on top of the diamond. Photoluminescence photons of the NV in the band greater than 680 nm are collected through an oil-immersion objective lens (Olympus, 60x, NA 1.35), counted by an avalanche photodiode (APD Excelitas SPCM) during a 330-ns gating window at the beginning of the spin readout pulse [81] and digitized by a counting card (FAST ComTec MCS6). The experiment is controlled by custom measurement software (Qudi [82]) that features a software interface to quantum algorithms generated by Qiskit [83].

To convert experimentally measured fluorescence to polarization $\langle\sigma_z\rangle_{\mathrm{NV1+2}}$, we perform every experiment twice with additional π pulses on both NVs. The difference Δ_{alt} of such alternating experiments is then normalized to the optical contrast $\mathrm{I}_{|00\rangle} - \mathrm{I}_{|11\rangle}$ between the fluorescence in states $|00\rangle$ and $|11\rangle$. Our measurement relates to the readout of a register state ρ as $\langle\sigma_z\rangle_{\mathrm{NV1+2}} = \Delta_{\mathrm{alt}}/(\mathrm{I}_{|00\rangle} - \mathrm{I}_{|11\rangle}) = R(\rho)$, with the readout outcome R as defined in Appendix B [21].

D. Simulations

For the simulation results of Fig. 4, we use the following Hamiltonian to describe the system of two NV centers in their orbital ground state $^3A_2$:

$$H(t) = H^0_{\mathrm{NV1}} + H^0_{\mathrm{NV2}} + H^{\mathrm{int}}_{12} + H^{\mathrm{mw}}(t), \tag{2}$$

where H^0_{NV1} and H^0_{NV2} are the single NV Hamiltonians, H^{int}_{12} the dipole-dipole coupling Hamiltonian, and H^{mw} the microwave Hamiltonian, which is, in general, time dependent. The single NV center Hamiltonians [84]

$$\begin{aligned} H^0 &= DS_z^2 + \vec{\omega}_{\mathrm{e}} \cdot \vec{S} + QI_z^2 + \vec{\omega}_{\mathrm{n}} \cdot \vec{I} + \vec{S}\,\underline{A}\,\vec{I} \\ &\text{with} \quad \vec{\omega}_{\mathrm{e/n}} \equiv -\gamma_{\mathrm{e/n}}\vec{B} \end{aligned} \tag{3}$$

contain the electron zero-field splitting D, the nuclear quadrupole moment Q, the Zeeman splitting due to the static magnetic field $\vec{B}$, the gyromagnetic ratio of the electron/nuclear spin in angular frequency units, $\gamma_{\mathrm{e/n}}$, and the hyperfine coupling to the ^{14}N nuclear spin via

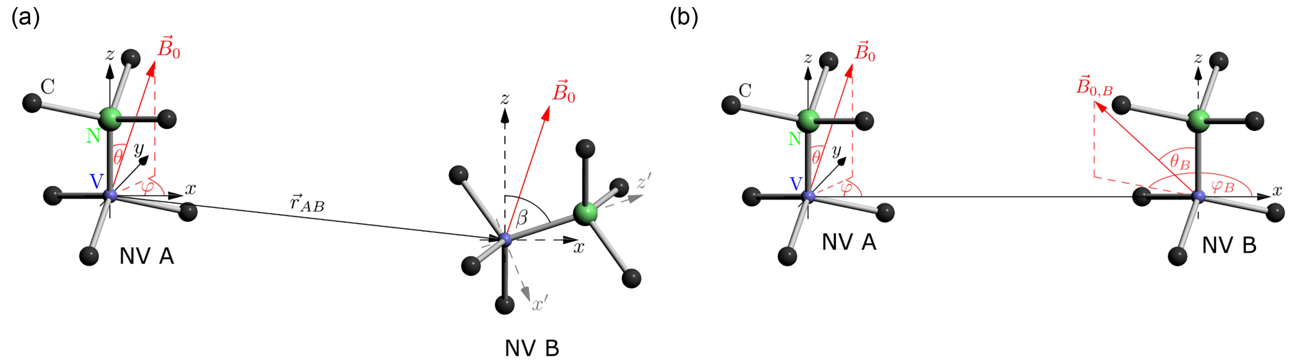

FIG. 5. Geometry of the two-NV quantum register. (a) Physical geometry of coupled NVs A and B in the crystal lattice, not to scale. The order in the gate sequence (labeled NV1 and NV2) is given, along with geometry parameters in Table I. (b) Effective picture of the coupling. In this case, each NV is subject to a (unphysical) different magnetic field vector and the dipolar coupling is of zz type.

the tensor $\underline{A}$. Both the electron spin (initialized in its ground state) and the ^{14}N nucleus (initialized in a maximally mixed state) are triplets: $S = I = 1$. The two NV centers have distinct crystal axes [cf. Fig. 5(a)], causing misalignment between the magnetic field and the NV axes and thus a logical basis that is given by rotated eigenstates.

For simulating the dynamics of the system, we use an effective dipole-dipole interaction (along the quantization axes) in the H_{12}^{int} term, which is described in detail in Appendix B, and list the employed estimates of the system parameters, such as the magnetic field and interaction strength in Appendix A. Decoherence is accounted for by applying a factor $(1 - \mathrm{EPC}_{T2})$ in Figs. 4(c) and 4(d), $(1 - \mathrm{EPG}_{T2})$ in Fig. 4(e), and $(1 - \mathrm{EPG}_{T2,1\mathrm{q}})$ for the single-qubit gates in Fig. 10(b). These factors, calculated in Sec. IV F, yield approximately constant decoherence contributions to the fidelities in the simulated Rabi frequency range.

In order to investigate the effect of the charge-state initialization SPAM error, we perform a numerical simulation that takes into account the probabilities that each of the NV centers is initially prepared in either the NV$^-$ or NV^0 charge state. This simulation employs the simplified Hamiltonian described in Appendix D and does not take into account the effect of decoherence. Thus, we include a phenomenological, single exponential decay of the observed signal in the charge-state simulations in Figs. 3(a) and 3(c), which is calibrated using the measured pEPGs of Figs. 3(b) and 3(d).

E. Repetitive benchmarking

To convert the measured repetitive benchmarking decays into (pseudo) gate errors, we assume a single exponential decay model that is known to well describe the usual $T_{2,\mathrm{XY8}}$ measurements on single NVs [85]. We express the decay in terms of the gate repetition number n as

$$y = y_0 + a * \exp(-n/N_d) = y_0 + a * p^n, \qquad (4)$$

where we used the identity $p = \exp[-(1/N_d)] = (1 - \mathrm{pEPG})$ to convert the gate decay parameters N_d, p into a gate error pEPG. The remaining free fit parameters are the amplitude a and the offset y_0.

Similarly, we obtain the T_2 limit decay curve in Fig. 3 by calculating the polarization loss per applied two-qubit gate of length $t_{\mathrm{gate}} = N_\pi \tau_1$ from the mean of the measured $T_{2,\mathrm{XY8}}$ of both NVs in Fig. 2(b):

$$p\mathrm{EPG}_{T2} = 1 - \exp(-t_{\mathrm{gate}}/((T_{2,\mathrm{XY8,NV1}} + T_{2,\mathrm{XY8,NV2}})/2)) \qquad (5)$$

We note that the pEPG derived here from the lifetime parameter of an exponential fit is a useful tool for easily implementable benchmarking, but the results are difficult to compare among experiments (which motivates our labeling as "pseudo" EPG). We empirically find a single exponential decay, which is also the decay model widely used in T_2 measurements [86]. While repetitive benchmarking is similar to T_2 experiments—except for the additional evolution by the dipolar coupling—the exact nature of the decay depends on the environment of the probed spins [85,87].

F. Randomized benchmarking

We use the same single exponential model of Eq. (4) to obtain a decay parameter p for the observed randomized benchmarking decays. If the gate dependency of the errors is small enough, the measured EPC becomes a good estimate of the average gate set infidelity [88],

$$\mathrm{EPC} = \frac{2^{\mathrm{n}} - 1}{2^{\mathrm{n}}}(1 - p) \approx \frac{\sum_i (1 - F_{\mathrm{avg}}(\tilde{C}_i, C_i))}{\sum_i 1}, \qquad (6)$$

where n is the number of qubits, $\{\tilde{C}_i\}$ are the Clifford gates and $\{C_i\}$ the respective ideal ones (to account for the possibility of gate-dependent errors [88]), and

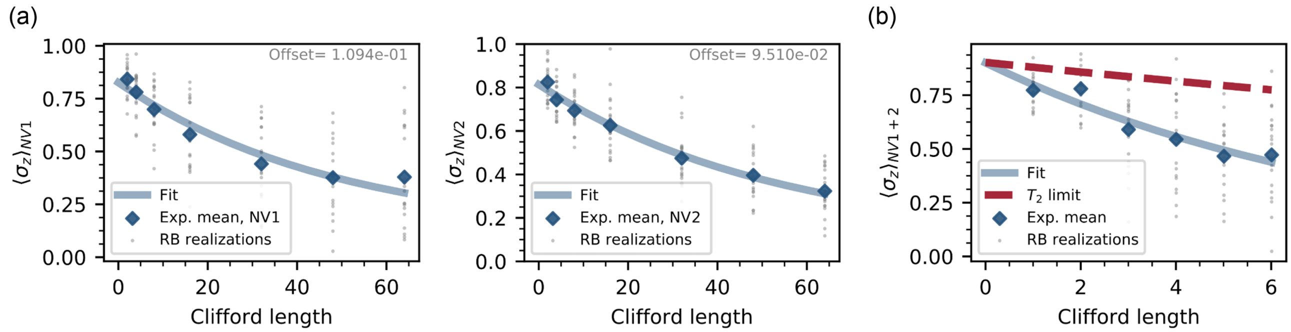

FIG. 6. Single-qubit randomized benchmarking. In panel (a), given the gate set $\mathrm{GPC}_{1\mathrm{q}} = 1.97$, we extract bare single-qubit gate fidelities of $F_{1\mathrm{q,NV1}} = (99.49 \pm 0.56)\%$ and $F_{1\mathrm{q,NV2}} = (99.53 \pm 0.49)\%$. Offset parameters are fixed by a separate measurement, as described in Sec. IV. (b) Average single-qubit error $F_{1\mathrm{q}} = (99.23 \pm 0.12)\%$ from modified two-qubit randomized benchmarking with a stripped entangling gate.

$$F_{\mathrm{avg}}(\tilde{C}_i, C_i) = \int d\psi Tr(\tilde{C}_i[|\psi\rangle\langle\psi|]C_i[|\psi\rangle\langle\psi|]) \quad (7)$$

is the overlap between the actual process of the i th Clifford $\tilde{C}_i$ and the ideal C_i. Here, F_{avg} is the average over all possible initial pure states ψ.

Our experiments are generated from the Qiskit software package using the gate set $\{\pi_x, (\pi/2)_x, \pi_y, (\pi/2)_y, \mathrm{C_1NOT_2}\}$ and 20 random experiments per Clifford. While the single-qubit rotations are easily realized on our NV hardware by microwave pulses with appropriate phases, we need to express $\mathrm{C_1NOT_2}$ in terms of our available $\sqrt{ZZ}$ gate and multiplication with single-qubit unitaries:

$$\begin{aligned}\mathrm{C_1NOT_2} &= \pi_{x,1} * (\pi/2)_{-y,2} * \sqrt{ZZ} * (\pi/2)_{x,1} \\ &* (\pi/2)_{y,2} * (\pi/2)_{y,1} * (\pi/2)_{-x,2} * (\pi/2)_{x,1}. \quad (8)\end{aligned}$$

After running Qiskit's automatic transpiler optimization ("Optimize1qGatesDecomposition") to reduce the number of single-qubit rotations in the gate string, we end up with a randomized benchmarking experiment that contains, on average, $\mathrm{GPC}_{1\mathrm{q}} = 10.5$ single-qubit $(\pi_x, (\pi/2)_x, \pi_y, (\pi/2)_y)$ and $\mathrm{GPC}_{2\mathrm{q}} = 1.8$ two-qubit ($\sqrt{ZZ}$) native gates per Clifford gate. The measured EPC, but not $F_{2\mathrm{q}}$, could be further improved by finding a more efficient gate set with smaller $\mathrm{GPC}_{1\mathrm{q}}$.

Two-qubit randomized benchmarking yields an EPC that is an average error over the whole gate set. For estimating the error of our $\sqrt{ZZ}$ gate, we use the EPC definition [83]:

$$\begin{aligned}\mathrm{EPC} &= 1 - \prod_i (1 - \mathrm{EPG}_i)^{GPC_i} \\ &= 1 - (1 - \mathrm{EPG}_{2\mathrm{q}})^{\mathrm{GPC}_{2\mathrm{q}}}(1 - \mathrm{EPG}_{1\mathrm{q}})^{\mathrm{GPC}_{1\mathrm{q}}}, \quad (9)\end{aligned}$$

where we collected all single-qubit gate errors in an average gate error $\mathrm{EPG}_{1\mathrm{q}}$. Solving for $\mathrm{EPG}_{2\mathrm{q}}$ allows us to estimate the two-qubit gate error from the measured two-qubit randomized benchmarking (yielding EPC) and the precharacterized average effective single-qubit error per Clifford $\mathrm{EPC}_{1\mathrm{q}} = 1 - (1 - \mathrm{EPG}_{1\mathrm{q}})^{\mathrm{GPC}_{1\mathrm{q}}}$ (data are given in Fig. 6).

Our randomized benchmarking uses the single exponential model in Eq. (4) as a decay model and yields results with low statistical uncertainty, if the tail of the decay curve is well captured. Because of limitations of the applicable microwave power, capturing the decay tail is not always possible in our experiment. For the two-qubit case, we thus determine the offset parameter y_0 of the decay separately first, by applying a high number of intentionally miscalibrated pulses, and then fix the decay offset parameter. This method amplifies gate errors and thus gives a value that equally represents the high error limit. We consistently observe $y_0 < 0.001$ in our experiments.

We observe that the randomized benchmarking decay lifetime in Fig. 4(b) is shorter than expected from repetitive benchmarking (factor $\mathrm{EPC}/\mathrm{EPC}_{T2} = 5.9 \pm 1.1$, $\overline{\mathrm{pEPG}}/\mathrm{pEPG}_{T2} = 2.5 \pm 1.2$, and coherence limit EPC_{T2} derived in Sec. IV). We attribute this observation to the fact that, in repetitive benchmarking, coherent errors are well refocused by the symmetric timing of the decoupling π pulses in the $\sqrt{ZZ}$ gate sequence. In combination with random single-qubit Clifford gates in randomized benchmarking, this decoupling works less efficiently.

From simulations, we find that a single exponential decay with offset $y_0 = 0$ well describes the behavior for experimentally accessible numbers of two-qubit Clifford gates. For $n_{\mathrm{cliff}} \gg 10$, accumulated crosstalk and leakage become more relevant, which can cause a slower, second exponential decay [89] and depolarization into equal populations of the three $m_s = 0, \pm 1$ sublevels.

1. Coherence limit

For the T_2 coherence limit in Fig. 4, we first estimate the error caused by decoherence per two-qubit gate assuming the same single exponential decay as in the repetitive benchmarking case; thus, $\mathrm{EPG}_{T2,2\mathrm{q}} = \mathrm{pEPG}_{T2} = 1.4\%$ [Eq. (5)]. The decoherence errors from single-qubit gates are much smaller, as they feature shorter gate lengths. Hence, we roughly estimate $\mathrm{EPG}_{T2,1q}$ by inserting the average single-qubit gate length into Eq. (5). Knowing the average number of gates per Clifford gate, we obtain the coherence limit per Clifford EPC_{T2} from Eq. (9).

Higher-order decoupling should enable prolonging T_2 towards the longer $2T_1$ limit. We thus estimate in Appendix H an achievable coherence limit for the $\sqrt{\mathrm{ZZ}}$ gate of $F_{2q} = 99.6\%$ at room temperature.

2. Relative error contributions

We extract the relative error contribution in randomized benchmarking [Fig. 4(d)] from the simulation as follows: First, we simulate the $\langle\sigma_z\rangle_{\mathrm{NV1+2}}$ outcome of the experiment at $n_{\mathrm{cliff}} = 2$ with all (coherent) error effects and multiply this value (z_{sim}) with the known EPC_{T2} to account for the decoherence of a single, average Clifford gate:

$$z_{\mathrm{sim},T_2} = z_{\mathrm{sim}}(1 - \mathrm{EPC}_{T2}). \tag{10}$$

Using the single exponential decay in Eq. (4), we convert the simulated outcome of the randomized benchmarking experiment to an average fidelity parameter p:

$$p_{\mathrm{full},T_2} = \sqrt[n_{\mathrm{cliff}}]{(z_{\mathrm{sim},T_2} - y_0)/a}, \tag{11}$$

where we take the SPAM parameters a, y_o from the measurement in Fig. 4(a).

The deviation of our simulation (in terms of p) including all errors from a perfect, gate-error-free experiment with $p = 1$ is

$$\begin{aligned} \Delta_{\mathrm{full},T_2} &= 1 - p_{\mathrm{full},T_2} \\ \Delta_{Er_i,T_2} &= 1 - p_{Er_i,T_2}. \end{aligned} \tag{12}$$

Similarly, we obtain average fidelity parameters p_{Er_i,T_2} and deviations Δ_{Er_i,T_2} for turning off specific error sources Er_i. Then, the relative contribution $c_r(Er_i)$ is given by the difference between full simulation and the improved result without this error source p_{Er_i,T_2} divided by the swing of the full experiment:

$$\begin{aligned} c_r(Er_i) &= \frac{p_{Er_i,T_2} - p_{\mathrm{full},T_2}}{\Delta_{\mathrm{full,T_2}}} \\ &= 1 - \Delta_{Er_i,T_2}/\Delta_{\mathrm{full},T_2} \end{aligned} \tag{13}$$

For example, when the error Er_i is turned off and the result p_{Er_i,T_2} does not change, the error contribution is $c_r(Er_i) = 0$.

Ideally, we would quantify the error introduced by an off-axis magnetic field by comparing it to the application of parallel magnetic fields of different strength on both NVs in simulation. However, the exact transition frequencies that are asymmetrically distributed around the ZFS can only be recovered with a misaligned magnetic field in the simulation. Instead, we note that the experimental outcome on the electron spin with a polarized nitrogen spin is equivalent to the case where the hyperfine interaction is turned off completely because no population transferring terms $A_{ij}S_i \otimes I_j$, $i \neq j$ exist in $\underline{A}$ for a perfectly aligned magnetic field. Hence, we can attribute the additional error that occurs for the polarized nitrogen-spin case when $A_{ij}S_i \otimes I_j$, $i \neq j$ terms are present solely to the misaligned magnetic field:

$$c_r(\vec{B}\perp\vec{e}_z) = \mathrm{c_r(HFS)} - c_r(\mathrm{unpol.}^{14}\mathrm{N}). \tag{14}$$

Finally, we can turn off all known error sources in the simulation simultaneously—crosstalk, leakage, and the hyperfine interaction—and calculate the difference from an experiment with only decoherence:

$$c_r(\mathrm{residual}) = (1 - c_r(T_2)) - \mathrm{c_r(HFS, ct + leak)}. \tag{15}$$

These small residual errors scale with the microwave power in a range of $c_r(\mathrm{residual}) = [0.9\% - 0.09\%]$ for the studied Rabi frequencies between 5 and 30 MHz. Thus, we attribute them mainly to unwanted dipolar interaction occurring during the microwave pulses.

Some part of the gate infidelity cannot be attributed to a single error. This cumulative effect increases in parallel with crosstalk and leakage but has a small contribution (7%) at the experimental setting.

The alternating readout described above for conversion from fluorescence to the spin state can reject some of the leakage error. Although we verified in simulations that this effect is small for our magnetic field setting 2, we base Fig. 4(d) on a simulation without the additional π pulses in order to not underestimate leakage.

Our simulation of randomized benchmarking in Fig. 4(c) does not account for experimental SPAM errors like the imperfect charge-state initialization or mixing of the initialized spin state. Such SPAM errors do not change the decay parameter p in randomized benchmarking, but it will be represented in the amplitude fit parameters y_0, a. Hence, we use a free parameter that is multiplied onto our simulation result $\langle\sigma_z\rangle_{\mathrm{NV1+2}}$ and that is determined by least-square minimization of the difference from the experimental data.

G. Error bars

Error bars on experimental fluorescence data are estimated from the photon shot noise as $1/\sqrt{n_{\mathrm{phot}}}$ and are error propagated to the spin state domain. Errors on parameters extracted from fits are 1σ uncertainties.

ACKNOWLEDGMENTS

We thank Michael Olney-Fraser, Thomas Unden, Philipp Neumann, and Alex Retzker for helpful discussions.

T. J. acknowledges support by the Foundation of German Business (sdw). This work was funded by the German Federal Ministry of Research (BMBF) through future cluster QSENS to Project No. 03ZU2110DB and projects DE-Brill (No. 13N16207), SPINNING (No. 13N16210, No. 13N16209, and No. 13N16215), CoGeQ (No. 13N16101), DIAQNOS (No. 13N16463), quNV2.0 (No. 13N16707), Quamapolis (No. 13N15375), Quantenrepeater.Net (QR.N), EXTRASENS (No. 13N16935), and QuantumHiFi (No. 16KIS1593); DLR via Project QUASIMODO (No. 50WM2170); and Deutsche Forschungsgemeinschaft (DFG) via Project No. 386028944, No. 445243414, No. 387073854, No. 491245864, No. 546850640, and No. 554644981. This project has also received funding from the European Union's HORIZON Europe program via projects QuMicro (No. 101046911), SPINUS (No. 101135699), C-QuENS (No. 101135359), QCIRCLE (No. 14 101059999), and FLORIN (No. 101086142); European Research Council (ERC) via Synergy grant HyperQ (No. 856432); and Carl-Zeiss-Stiftung via the Center of Integrated Quantum Science and technology (IQST) and project Utrasens-Vir (No. P2022-06-007). Additional support was provided by JSPS KAKENHI (No. 21H04646 and No. 24K01286), JST Moonshot R&D Grant No. JPMJMS2062, MEXT Q LEAP Grant No. JPMXS0118067395, JST Adopting Sustainable Partnerships for Innovative Research Ecosystem (ASPIRE) via Grant No. JPMJAP24C1.

T. J., P. J. V., M. M. M., and F. J. conceived the experiment. T. T. and S. O. fabricated the sample, and T. J., R. S., and S. O. prepared and characterized the sample. T. J. wrote the code for the experiment and performed the measurements for the presented experimental data. F. F. and G. G. developed and analyzed the model and performed the simulations. T. J., F. F., and G. G. analyzed the data and wrote the manuscript. R. S. S., G. G., J. Z., S. O., T. C., M. M. M., and F. J. supervised the project. All authors reviewed and contributed to the manuscript.

The authors declare no competing interests.

DATA AVAILABILITY

Some of the data that support the findings of this article are openly available [90]. Datasets are not publicly available. The data are available from the authors upon reasonable request.

APPENDIX A: MAGNETIC FIELD PARAMETERS

Most data presented are measured at the optimized magnetic field setting 2 of Table I. There, we use an aligned magnetic field on the control qubit (NV2) for minimal interaction with the nitrogen nuclear spins. On the misaligned target qubit, the interaction during the entangling gate is more pronounced, but we can use the τ_1 degree of freedom to mitigate the issue (see Appendix D). In Fig. 4(b), we also use the unoptimized setting 1 to illustrate the strong influence that microwave crosstalk and leakage can have.

To obtain the magnetic field geometries, we determine the microwave transition frequencies by an ODMR measurement. For each magnetic field setting, the ODMR of two NV centers yields a set of four transition frequencies, where the lowest and highest frequencies form a pair as well as the two frequencies in between, which are associated with a magnetic field of higher misalignment with the NV center axis. Given these transition frequencies and the zero-field splitting D, one is able to calculate the absolute magnetic field value $\omega_{e,i}/(2\pi)$ (in frequency units) and the misalignment with each NV center using [91]

$$\left(\frac{\omega_{e,i}}{2\pi}\right)^2 = \frac{1}{3}\left(f_{1,i}^2 + f_{2,i}^2 - f_{1,i}f_{2,i} - \left(\frac{D_i}{2\pi}\right)^2\right) - \left(\frac{E_i}{2\pi}\right)^2, \tag{A1}$$

$$H_i = \frac{7(\frac{D_i}{2\pi})^3 + 2(f_{1,i} + f_{2,i})(2(f_{1,i}^2 + f_{2,i}^2) - 5f_{1,i}f_{2,i} - 9(\frac{E_i}{2\pi})^2) - 3(\frac{D_i}{2\pi})(f_{1,i}^2 + f_{2,i}^2 - f_{1,i}f_{2,i} + 9(\frac{E_i}{2\pi})^2)}{9(f_{1,i}^2 + f_{2,i}^2 - f_{1,i}f_{2,i} - (\frac{D_i}{2\pi})^2 - 3(\frac{E_i}{2\pi})^2)}, \tag{A2}$$

$$\cos(2\theta_i) = \frac{H_i - E_i/(2\pi)\cos(2\varphi_i)}{D_i/(2\pi) - E_i/(2\pi)\cos(2\varphi_i)}, \tag{A3}$$

where we defined H_i for a clear notation, $f_{1,i}$ and $f_{2,i}$ are the mentioned pair of transition frequencies, θ_i is the misalignment angle between the axis of the considered NV center and the magnetic field, φ_i is the azimuthal angle (in the plane perpendicular to the NV axis), and $i \in A, B$ is the NV center to which the quantities are assigned. Note that the geometry in Fig. 5(a) is defined in terms of the physical NVs A and B, which can differ from their order in the gate sequence (NV1 and NV2).

Crystal strain can be divided into transversal strain E_i and axial strain, which we model by including it in the zero-field parameters D_i [92]. Distinguishing both components from ODMR-like experimental data is not straightforward if considering a system of two NVs. Thus, we use the following methodology to determine D_i, E_i, making use of the assumption that the (absolute value of the) external magnetic field is constant for the closely located NVs.

As E_i is typically small (much less than 1 MHz) in bulk samples [92–94], we set it to zero. For the magnetic field setting 2, we observe that Eqs. (A1)–(A3) do not lead to a physical solution when assuming a typical zero-field splitting at room temperature of $D/(2\pi) = 2870$ MHz [81]. Thus, we obtain the solution $D_A/(2\pi) = 2865.42$ MHz, which minimizes the absolute value of the axial strain on NV A and yields a valid magnetic field vector. Under the constraint that the absolute magnetic field is the same for both NV centers, we find an axial strain for NV B of $D_B/(2\pi) = 2867.27$ MHz. Our results for D_A, D_B are not significantly altered if a (pessimistic estimate) transversal strain of $E/(2\pi) \sim 1$ MHz [95] is introduced, justifying our initial assumption of $E = 0$.

Using the same D_A, D_B obtained from the analysis of magnetic field setting 2, in the lower magnetic field setting 1, we observe a small difference in the absolute magnetic field of both NVs, $|\omega_{e,A} - \omega_{e,B}|/\gamma_e = 1.1\ G$.

We simplify our notation and use $\theta \equiv \theta_A$ and $\varphi \equiv \varphi_A$ in the following. Given the previously determined magnetic field misalignment θ_i, we can calculate the remaining angle φ in Fig. 5(a) by making use of simple geometry. The angle between the direction of the magnetic field $\hat{\vec{\omega}}_e$ and the axis of NV center B, $\hat{\vec{n}}_B = (\sin\beta, 0, \cos\beta)^T$, is the misalignment angle θ_B:

$$\hat{\vec{\omega}}_e = \hat{\vec{B}} = (\cos\varphi\sin\theta, \sin\varphi\sin\theta, \cos\theta)^T$$
$$\cos\theta_B = \hat{\vec{\omega}}_e^T \cdot \hat{\vec{n}}_B = \cos\varphi\sin\theta\sin\beta + \cos\theta\cos\beta \qquad \text{(A4)}$$

Note that we can find φ up to a relative minus sign, which cannot be determined in a system of two NV centers only, due to its symmetry. At the same time, as we cannot differentiate between the signs, we do not expect that the dynamics are affected by the choice of sign.

Similarly, the geometry is not uniquely defined for θ, with two solutions θ and $\theta_i' = \pi - \theta_i$ for $\theta \in [0, \pi)$.

Furthermore, the angle between the NV center axes can take two possible values, $\beta' = 109.47°$ and $\beta = 180° - \beta' = 70.53°$, due to the crystal structure of diamond.

APPENDIX B: SIMULATION OF TWO INTERACTING NV CENTERS

1. System Hamiltonian

We start with the Hamiltonian [84] of a single, negatively charged, NV center with an inherent nitrogen ^{14}N nucleus in its orbital ground state $^3A_2$:

$$H^0 = \underbrace{DS_z^2 + \vec{\omega}_e \cdot \vec{S}}_{\equiv H^e} + \underbrace{QI_z^2 + \vec{\omega}_n \cdot \vec{I}}_{\equiv H^n} + \underbrace{\vec{S}\,\underline{A}\,\vec{I}}_{\equiv H^{hfc}}, \qquad \text{(B1)}$$

where D is the electronic zero-field splitting; Q the nuclear quadrupole moment; $\underline{A}$ the hyperfine tensor, which is diagonal; and $\vec{\omega}_{e/n} \equiv -\gamma_{e/n}\vec{B}$, with $\gamma_{e/n}$ being the gyromagnetic ratio of the electron/nuclear spin in angular frequency units (Hz rad/T) and $\vec{B}$ the magnetic field at the positions of the NV center. In the chosen coordinate system, the z axis is aligned with the NV center axis. Throughout this work, we use Hamiltonians in angular frequency units, i.e., $\hbar = 1$.

We call $H^{e/n}$ the electron/nuclear Hamiltonian and H^{hfc} the hyperfine coupling Hamiltonian. The respective spin operators $S_i(I_i)$, with $i \in \{x, y, z\}$, are defined to act on the electron (nuclear) states of the NV center only. For example, S_z is equivalent to $S_z \otimes \mathbb{1}$, i.e., a Kronecker product of S_z for NV1 and the identity operator $\mathbb{1}$ for the nucleus. Both the electron spin, due to the charge-state NV$^-$ of the NV center, and the nuclear spin, since we consider the ^{14}N isotope, are triplets ($S = I = 1$).

The system under consideration consists of two NV centers with distinct crystal axes [Fig. 5(a) sketches magnetic field setting 2 (Table I), in which NV1 is more strongly misaligned], interacting with each other via dipole-dipole coupling; they are exposed to a static magnetic field and microwave pulses of arbitrary shape. Note that this section is written with respect to magnetic field setting 2. The labels NV1 and NV2 that indicate the order in the gate sequence would need to be switched for magnetic field setting 1.

The free Hamiltonian of the system is given by

$$H^{free} = H^0_{NV1} + H^0_{NV2} + H^{int}_{12} \qquad \text{(B2)}$$

with the dipole-dipole interaction Hamiltonian H^{int}_{12},

$$H^{int}_{12} = g_0(r_{12})[\vec{S}_1 \cdot \vec{S}_2 - 3(\vec{S}_1 \cdot \hat{\vec{r}}_{12})(\vec{S}_2 \cdot \hat{\vec{r}}_{12})]$$
$$= g_0(r_{12})\vec{S}_1\underline{G}(\hat{\vec{r}}_{12})\vec{S}_2', \qquad \text{(B3)}$$

where we defined $\vec{S}_k$ as the operator $\vec{S}$ acting on the kth NV center ($k = 1, 2$) and its components $S_{i,k}(i = x, y, z)$. The rotation of the spin operator $\vec{S}_2'$ of NV2 is detailed below.

We denote the displacement of NV center 1 from NV center 2 as $\vec{r}_{12}$ and the absolute coupling strength as $g_0(r_{12})$, depending on the distance r_{12} between the NV centers:

$$g_0(r_{12}) \equiv \frac{\mu_0}{4\pi}\frac{\hbar\gamma_e^2}{r_{12}^3}. \qquad \text{(B4)}$$

We call $\underline{G}(\hat{\vec{r}}_{12})$ the geometric tensor. It does not depend on the distance r_{12} but rather on the normalized relative position vector $\hat{\vec{r}}_{12}$ [cf. Fig. 5(a)].

The two NV centers have misaligned axes; i.e., the crystal axis of NV1 is rotated by an angle β around the y

axis with respect to the axis NV2 [cf. Fig. 5(a)]. As a result, the Hamiltonian takes an unhandy shape; e.g., the zero-field splitting term reads $D(\cos(\beta)S_z + \sin(\beta)S_x)^2$. We solve this problem by transforming the frame of NV1: We rotate the spin operators and fields of NV1 around the y axis by an angle $-\beta$ into the x', y', z' frame, where the axis of NV1 coincides with the z' axis [cf. Fig. 5(a)]:

$$\vec{\omega}' = R_y(-\beta)\vec{\omega}, \quad \vec{S}' = R_y(-\beta)\vec{S},$$
$$\vec{S} \equiv \begin{pmatrix} S_x \\ S_y \\ S_z \end{pmatrix}, \quad R_y(-\beta) = \begin{pmatrix} \cos\beta & 0 & -\sin\beta \\ 0 & 1 & 0 \\ \sin\beta & 0 & \cos\beta \end{pmatrix}. \tag{B5}$$

In the primed frame, the Hamiltonian of NV1 again takes the usual form as given in Eq. (B1); i.e., the zero-field splitting term reads $D(S_z')^2$. In this picture, the NV centers experience a different magnetic field and a modified geometric tensor $\underline{G}(\hat{\vec{r}}_{12})$.

As the NV centers are exposed to a constant magnetic field that is (generally) misaligned with their crystal axes, their quantization axes change (in length and direction), which results in new eigenvalues and eigenstates $(|g\rangle, |e_1\rangle, |e_2\rangle)$ of the Hamiltonian. As a consequence, the eigenstates of the electron Hamiltonian H^{e} do not coincide with the eigenstates of the $S_{z,2}, S'_{z,1}$ operators, but we can define new spin operators $\tilde{S}_{z,2}, \tilde{S}'_{z,1}$ that have the same eigenstates as H^{e} and take the usual (matrix) form in the corresponding basis. Similarly, we define $\tilde{S}_{x/y,2}, \tilde{S}'_{x/y,1}$.

The dipole-dipole interaction is (typically) small compared to the electron transition frequencies ($g_0 \ll \omega_i$), so a secular approximation can be applied, whereby small, nondiagonal elements (in the basis of the $\tilde{S}_{z,i}$ eigenstates) in the dipole-dipole interaction Hamiltonian are neglected. This process simplifies the dipole-dipole coupling to

$$H_{12}^{\mathrm{int}} = g(\vec{r}_{12}, \beta, \vec{B})\tilde{S}_{z,2}\tilde{S}'_{z,1}, \tag{B6}$$

where $g(\vec{r}_{12}, \beta, \vec{B})$ is the effective coupling strength [$v_{\mathrm{dip}} = g/(2\pi)$ in frequency units].

By transforming the frame of NV center 1, transforming the spin operators into the basis of the electron eigenstates, and performing the secular approximation, we have developed an effective picture of the two-NV-center system [cf. Fig. 5(b)].

The total (noiseless) Hamiltonian is given by

$$H_{\mathrm{driven}}(t) = H^{\mathrm{free}} + H^{\mathrm{mw}}(t), \tag{B7}$$

where H_{NV1}^0 and H_{NV2}^0 are the single NV center Hamiltonians of NV centers 1 and 2, and H^{mw} the microwave Hamiltonian,

$$H^{\mathrm{mw}}(t) = \sum_{i=1,2} \sqrt{2}[\Omega_{i,x}(t)\cos(\omega_i t + \xi_i) + \Omega_{i,y}(t)\sin(\omega_i t + \xi_i)]H^{\mathrm{control}}. \tag{B8}$$

Here, $\Omega_{i,x}(t)$ and $\Omega_{i,y}(t)$ are time-dependent amplitudes (or control functions) that vary only slowly compared to the angular carrier frequencies ω_i. Phases of the carrier, generally set to zero, are denoted ξ_i, and H^{control} is the control Hamiltonian,

$$H^{\mathrm{control}} \equiv \tilde{S}'_{x,1} + \tilde{S}_{x,2} + \tilde{\gamma}(I_{x,1} + I_{x,2}), \tag{B9}$$

with $\tilde{\gamma} \equiv \gamma_{\mathrm{n}}/\gamma_{\mathrm{e}} = \omega_{\mathrm{n}}/\omega_{\mathrm{e}}$.

2. Simulation

For simulating the time dynamics of the system, we start with single NV Hamiltonians $H_{1/2}^0$, with the rotation by angle $-\beta$ applied on NV center 1, as above, and we compute the matrix T that diagonalizes the sum of the electron Hamiltonians $H^{\mathrm{e}} \equiv H_1^{\mathrm{e}} + H_2^{\mathrm{e}}$, such that $T^\dagger H^{\mathrm{e}} T$ is diagonal.

We apply the diagonalization matrix to the sum of the single NV Hamiltonians $H_1^0 + H_2^0$ and then add the effective dipole-dipole coupling term in Eq. (B4) to obtain the (effective) free Hamiltonian,

$$H_{\mathrm{free}} = T^\dagger(H_1^0 + H_2^0)T + H_{12}^{\mathrm{int}}. \tag{B10}$$

From here on, we use the basis of the electronic eigenstates, so $H_{12}^{\mathrm{int}} = g\tilde{S}_{z,2}\tilde{S}'_{z,1}$ as above.

The spin operators are defined as

$$\tilde{S}_{i,2} = S_i \otimes \mathbb{1} \otimes \mathbb{1} \otimes \mathbb{1}, \quad \tilde{S}'_{i,1} = \mathbb{1} \otimes \mathbb{1} \otimes S_i \otimes \mathbb{1}$$
$$I_{i,2} = \mathbb{1} \otimes I_i \otimes \mathbb{1} \otimes \mathbb{1}, \quad I_{i,1} = \mathbb{1} \otimes \mathbb{1} \otimes \mathbb{1} \otimes I_i \tag{B11}$$

with order (NV2, nuclear spin 2, NV1, nuclear spin 1) and

$$S_x = \frac{1}{\sqrt{2}}\begin{pmatrix} 0 & 1 & 0 \\ 1 & 0 & 1 \\ 0 & 1 & 0 \end{pmatrix} = I_x,$$
$$S_y = \frac{i}{\sqrt{2}}\begin{pmatrix} 0 & -1 & 0 \\ 1 & 0 & -1 \\ 0 & 1 & 0 \end{pmatrix} = I_y,$$
$$S_z = \begin{pmatrix} 1 & 0 & 0 \\ 0 & 0 & 0 \\ 0 & 0 & -1 \end{pmatrix} = I_z \tag{B12}$$

If the magnetic field is static, the Hamiltonian of the system is given by H_{free}, and therefore, it is time independent. In this case, the time evolution operator is calculated via the matrix exponential $U(t) = \exp(-iH_{\mathrm{free}}t)$ and then transformed into the rotating frame via

$$U_{\mathrm{rot}}(t) = V^{\dagger}(t)U(t) \quad \text{with} \quad V(t) = \exp(-iH_{\mathrm{trans}}t), \tag{B13}$$

where $H_{\mathrm{trans}} \equiv \omega_1(\tilde{S}'_{z,1})^2 + \omega_2(\tilde{S}_{z,2})^2$ is the Hamiltonian that generates the rotating frame transformation and $\omega_{1/2} = 2\pi f_{1/2}$ are the angular carrier frequencies, ideally coinciding with the transition lines $2\pi f_{\mathrm{i}}$ of the chosen qubit system (Table I).

If microwave pulses are applied, the Hamiltonian in Eq. (B7) contains time-dependent terms. In order to calculate the time evolution from t_0 to t, we approximate the time evolution via the Riemann summation method, whereby we evaluate the Hamiltonian at N discrete time points:

$$U(t, t_0) = \mathcal{T}\exp\left(-\mathrm{i}\int_{t_0}^{t} H_{\mathrm{rot}}(t')\mathrm{d}t'\right) \approx e^{-iH_{\mathrm{rot}}(t_N)\tau}\ldots e^{-iH_{\mathrm{rot}}(t_2)\tau}e^{-iH_{\mathrm{rot}}(t_2)\tau} \tag{B14}$$

with $t_j = t_0 + j\tau$ and $\tau = (t - t_0)/N$, where $N = 100$ GHz$(t - t_0)$ and $\mathcal{T}$ is the time ordering operator.

To realize faster convergence, i.e., realize the same precision with larger time steps, the Hamiltonian is transformed into the rotating frame (at every timestep) in which the Hamiltonian varies only slowly:

$$H_{\mathrm{rot}}(t_i) = V_i^{\dagger}(H_{\mathrm{driven}}(t_i) - H_{\mathrm{trans}})V_i \quad \text{with} \quad V_i = V(t_i). \tag{B15}$$

When dealing with sequences of pulses and free evolution, we multiply the respective unitaries time orderly.

Readout results $R(\rho)$ are obtained via the POVM element $E_g(\{\alpha_i\})$, similar to the definition in Ref. [21], as

$$R(\rho) = \mathrm{Tr}_{\mathrm{e}}[E_g \mathrm{Tr}_{\mathrm{n}}(U\rho U^{\dagger})] - \mathrm{Tr}_{\mathrm{e}}[E_g \mathrm{Tr}_{\mathrm{n}}(X_{12}U\rho U^{\dagger}X_{12}^{\dagger})]$$
$$E_g(\{\alpha_i\}) = \frac{1}{\alpha_1 + \alpha_2}(\alpha_1|g\rangle\langle g| \otimes \mathbb{1} + \alpha_2\mathbb{1} \otimes |g\rangle\langle g|) \tag{B16}$$

where X_{12} is a π_x pulse on NV center 1, followed by a π_x pulse on NV center 2, $\mathrm{Tr}_{\mathrm{e/n}}$ is the trace of the electron/nuclear spins, and $\alpha_{1/2}$ is a contrast parameter, proportional to the spin contrast observed in experiment.

As we only read out diagonal elements in the measurement, the results are the same in the rotating frame as in the lab frame (since V_i is diagonal).

Within the simulation, if not stated otherwise, the electron state is perfectly initialized in the ground state and the nuclear state in the maximally mixed state (thermal state approximation). If the nuclear state is initialized, then it is initialized into its $m_I = 0$ state.

If not stated otherwise, the pulses are chosen to have a sinusoidal shape. For example, for a π_x pulse on NV center 1, the control functions are given by

$$\Omega_{1,x}(t) = \Omega_{\max}\sin(\pi \cdot t/t_{\pi}),$$
$$\Omega_{1,y}(t) = \Omega_{2,x}(t) = \Omega_{2,y}(t) = 0, \tag{B17}$$

where $\Omega_{\max} = (\pi/2)\Omega_{\mathrm{Rabi}}$ is the peak amplitude of the envelope, $\Omega_{\mathrm{Rabi}} = (\pi/t_{\pi})$, and t_{π} is the π pulse duration of the sine-shaped pulse.

For evaluations of the gate fidelity, we use the definition of the average fidelity, given in Ref. [96]:

$$F_{\mathrm{avg}} = \frac{1}{d(d+1)}\sum_{i,j=1}^{d}(\langle i|G^{\dagger}\mathcal{D}(|i\rangle\langle j|)G|j\rangle + \langle i|G^{\dagger}\mathcal{D}(|j\rangle\langle j|)G|i\rangle), \tag{B18}$$

where G is the target quantum gate and $\mathcal{D}$ is the dynamical map, i.e., the time evolution of the electron spins (under the influence of the nuclear spins):

$$\mathcal{D}(\rho) = \mathrm{Tr}_{\mathrm{n}}(U\rho U^{\dagger}). \tag{B19}$$

In our case, $d = 4$, and the $\{|i\rangle\}$ states are the basis of the qubit subspace. We evaluate the gate fidelity in the rotating frame.

The randomized benchmarking circuits, used in the simulation, are the same as in the corresponding experiments. When sweeping the Rabi frequency, the set of pulses and the free evolutions are calculated for each Rabi frequency individually. When crosstalk and leakage are stated to be turned off, the control Hamiltonian is modified to only act on the qubit levels of the desired NV center.

APPENDIX C: SINGLE-QUBIT RANDOMIZED BENCHMARKING

To estimate the entangling gate fidelity $\mathrm{EPG}_{2\mathrm{q}}$ from the measured EPC of the gate set, we need to separate the error contribution of the single-qubit gates, as described in Sec. IV:

$$\mathrm{EPC} = 1 - (1 - \mathrm{EPG}_{2\mathrm{q}})^{\mathrm{GPC}_{2\mathrm{q}}}(1 - \mathrm{EPG}_{1\mathrm{q}})^{\mathrm{GPC}_{1\mathrm{q}}}, \tag{C1}$$

which is often done by measuring single-qubit randomized benchmarking on the subsystems [Fig. 6(a)]. Because of a particularity of our system, we take a slightly different approach here. We first note that, because of limitations of our microwave hardware, we never apply pulses on both NVs at the same time. As a result of the unpolarized nitrogen spins, a single-qubit rotation on NV1 can thus cause an unwanted phase pickup during the free evolution on NV2 and vice versa. This effect is neglected when carrying our single-qubit randomized benchmarking on a single NV only.

To obtain a one-qubit fidelity that represents all errors that are present when using the two-qubit register, we determine an average effective single-qubit error $\mathrm{EPC}_{1\mathrm{q}} = 1 - (1 - \mathrm{EPG}_{1\mathrm{q}})^{\mathrm{GPC}_{1\mathrm{q}}}$ from a modified two-qubit randomized benchmarking experiment in Fig. 6(b): This approach excludes all entangling gates from the generated experiment ($\mathrm{GPC}_{2\mathrm{q}} = 0$) and appends single-qubit correction pulses to revert to the ground state (resulting modified $\mathrm{GPC}_{1\mathrm{q}} = 11.5$). On every qubit, the modified experiment retains a random sequence of single-qubit Clifford operations—except for the free evolution that we treat as an error. We then extract the average effective single-qubit error $\mathrm{EPC}_{1\mathrm{q}}$ from the fitted decay lifetime parameter $p = \exp[-(1/N_d)]$ as

$$\mathrm{EPC}_{1\mathrm{q}} = (2^{\mathrm{n}} - 1)/2^{\mathrm{n}}(1 - p) = 0.085 \pm 0.013, \tag{C2}$$

with n the number of qubits in the Clifford sequence (here, $\mathrm{n} = 2$). This case translates to an effective single-qubit gate fidelity of $F_{1\mathrm{q}} = (99.23 \pm 0.12)\%$.

APPENDIX D: ENTANGLING GATE DYNAMICS AND CALIBRATION

In order to calibrate the duration of our entangling gate, we first analyze how it scales with the duration of our decoupling sequence and the choice of τ_1 and τ_2.

To this end, we simplify the effective model Hamiltonian [Eqs. (B2) and (B7)] further by treating the effect of the nitrogen nuclear spin as effective detuning (similarly to Ref. [97]), and we arrive at

$$\begin{aligned} H &= H^0_{\mathrm{NV1}} + H^0_{\mathrm{NV2}} + H^{\mathrm{mw}} + H^{\mathrm{int}}_{12} \\ H^0_{\mathrm{NV1}} &= DS^2_{z,1} + \Delta_1 S_{z,1} \\ H^0_{\mathrm{NV2}} &= DS^2_{z,2} + \Delta_2 S_{z,2} \\ H^{\mathrm{mw}} &= \sqrt{2}\{\Omega_{1,x}(t)\cos(\omega_1 t + \xi_1) \\ &\quad + \Omega_{2,x}(t)\cos(\omega_2 t + \xi_2)\}(S_{x,1} + S_{x,2}) \\ H^{\mathrm{int}}_{12} &= gS_{z,2}S_{z,1}. \end{aligned} \tag{D1}$$

Here, we consider the effective dipolar coupling $g = 2\pi\nu_{\mathrm{dip}}$ between the NV centers [98], with the zero-field splitting D of the NVs, and Δ_k, $k = 1, 2$ the effective detuning due to the Zeeman and hyperfine splittings, whose effect is typically refocused after the gate. Note that $\Omega_{1,x}(t)$ and $\Omega_{2,x}(t)$ characterize the Rabi frequencies of the microwave fields with angular frequencies ω_1 and ω_2 and initial relative phases ξ_1 and ξ_2, which we use to drive the two NV centers during the refocusing pulses. We use the operator labels $S_{z,1}$ and $S_{z,2}$ for $\tilde{S}'_{z,1}$ and $\tilde{S}_{z,2}$ from Appendix B 2, respectively, for simplicity of presentation and without loss of generality.

We move to the rotating frame, defined by $\omega_1 S^2_{z,1}$ and $\omega_2 S^2_{z,2}$; apply the rotating wave approximation, using $\Omega_{1,2}(t) \ll \omega_{1,2}$; and obtain

$$\begin{aligned} H^{\mathrm{NV1}}_{\mathrm{rot}} &= (D - \omega_1)S^2_{z,1} + \Delta_1 S_{z,1} + \frac{\Omega_1(t)}{\sqrt{2}} S_{x,1} = \begin{pmatrix} D - \omega_1 + \Delta_1 & \frac{\Omega_1(t)}{2} & 0 \\ \frac{\Omega_1(t)}{2} & 0 & \frac{\Omega_1(t)}{2} \\ 0 & \frac{\Omega_1(t)}{2} & D - \omega_1 - \Delta_1 \end{pmatrix} \\ &= \begin{pmatrix} \delta_1 & \frac{\Omega_1(t)}{2} & 0 \\ \frac{\Omega_1(t)}{2} & 0 & \frac{\Omega_1(t)}{2} \\ 0 & \frac{\Omega_1(t)}{2} & \delta\delta_1 \end{pmatrix} \end{aligned} \tag{D2}$$

$$\begin{aligned} H^{\mathrm{NV2}}_{\mathrm{rot}} &= (D - \omega_2)S^2_{z,2} + \Delta_2 S_{z,2} + \frac{\Omega_2(t)}{\sqrt{2}} S_{x,2} = \begin{pmatrix} D - \omega_2 + \Delta_2 & \frac{\Omega_2(t)}{2} & 0 \\ \frac{\Omega_2(t)}{2} & 0 & \frac{\Omega_2(t)}{2} \\ 0 & \frac{\Omega_2(t)}{2} & D - \omega_2 - \Delta_2 \end{pmatrix} \\ &= \begin{pmatrix} \delta\delta_2 & \frac{\Omega_2(t)}{2} & 0 \\ \frac{\Omega_2(t)}{2} & 0 & \frac{\Omega_2(t)}{2} \\ 0 & \frac{\Omega_2(t)}{2} & \delta_2 \end{pmatrix} \end{aligned} \tag{D3}$$

$$
H_{\mathrm{rot}}^{\mathrm{total}} = H_{\mathrm{rot}}^{\mathrm{NV1}} + H_{\mathrm{rot}}^{\mathrm{NV2}} + g\, S_{z,2}S_{z,1}
$$

$$
= \begin{pmatrix}
\delta_1+\delta\delta_2+g & \frac{\Omega_1(t)}{2} & 0 & \frac{\Omega_2(t)}{2} & 0 & 0 & 0 & 0 & 0 \\
\frac{\Omega_1(t)}{2} & \delta\delta_2 & \frac{\Omega_1(t)}{2} & 0 & \frac{\Omega_2(t)}{2} & 0 & 0 & 0 & 0 \\
0 & \frac{\Omega_1(t)}{2} & \delta\delta_1+\delta\delta_2-g & 0 & 0 & \frac{\Omega_2(t)}{2} & 0 & 0 & 0 \\
\frac{\Omega_2(t)}{2} & 0 & 0 & \delta_1 & \frac{\Omega_1(t)}{2} & 0 & \frac{\Omega_2(t)}{2} & 0 & 0 \\
0 & \frac{\Omega_2(t)}{2} & 0 & \frac{\Omega_1(t)}{2} & 0 & \frac{\Omega_1(t)}{2} & 0 & \frac{\Omega_2(t)}{2} & 0 \\
0 & 0 & \frac{\Omega_2(t)}{2} & 0 & \frac{\Omega_1(t)}{2} & \delta\delta_1 & 0 & 0 & \frac{\Omega_2(t)}{2} \\
0 & 0 & 0 & \frac{\Omega_2(t)}{2} & 0 & 0 & \delta_1+\delta_2-g & \frac{\Omega_1(t)}{2} & 0 \\
0 & 0 & 0 & 0 & \frac{\Omega_2(t)}{2} & 0 & \frac{\Omega_1(t)}{2} & \delta_2 & \frac{\Omega_1(t)}{2} \\
0 & 0 & 0 & 0 & 0 & \frac{\Omega_2(t)}{2} & 0 & \frac{\Omega_1(t)}{2} & \delta_2+\delta\delta_1+g
\end{pmatrix} \tag{D4}
$$

where we assume that the driving field frequency $\omega_1(\omega_2)$ is highly detuned from the transition frequencies of NV2 (NV1), so there is negligible crosstalk from pulses applied to NV1 on NV2 and vice versa. In addition, we take $\xi_1 = \xi_2 = 0$, for simplicity of presentation and without loss of generality. The matrix representation of $H_{\mathrm{rot}}^{\mathrm{NV1}}, H_{\mathrm{rot}}^{\mathrm{NV2}}$ is in the single-qutrit basis of each of the NV centers, while $H_{\mathrm{rot}}^{\mathrm{total}}$ is represented in the two-qutrit basis. In the experiment, the first driving field is approximately resonant with the $|0\rangle \leftrightarrow |+1\rangle$ transition on NV1 ($\delta_1 \equiv D - \omega_1 + \Delta_1 \ll \Omega_1(t), \delta\delta_1 \equiv D - \omega_1 - \Delta_1 \gg \Omega_1(t)$), and the second field is resonant with the $|0\rangle \leftrightarrow |-1\rangle$ transition on NV2 ($\delta_2 \equiv D - \omega_2 - \Delta_2 \ll \Omega_2(t), \delta\delta_2 \equiv D - \omega_2 + \Delta_2 \gg \Omega_2(t)$). The Hamiltonian elements, which characterize the evolution of the states, can effectively be addressed with the microwave fields (they do not have a very-high-frequency offset in the diagonal element of the Hamiltonian) as highlighted with dashed lines. Thus, the respective, reduced Hamiltonian, which characterizes the evolution that leads to our two-qubit gate, is given by

$$
H_{\mathrm{rot,reduced}}^{\mathrm{total}} = \begin{pmatrix}
\delta_1 & \frac{\Omega_1(t)}{2} & \frac{\Omega_2(t)}{2} & 0 \\
\frac{\Omega_1(t)}{2} & 0 & 0 & \frac{\Omega_2(t)}{2} \\
\frac{\Omega_2(t)}{2} & 0 & \delta_1+\delta_2-g & \frac{\Omega_1(t)}{2} \\
0 & \frac{\Omega_2(t)}{2} & \frac{\Omega_1(t)}{2} & \delta_2
\end{pmatrix}. \tag{D5}
$$

The detunings δ_1 and δ_2 typically cause dephasing but can be refocused by applying dynamical decoupling. The $z-z$ coupling g allows us to apply the $\sqrt{ZZ}$ gate, as evident from the analysis below. The Hamiltonian during free evolution, without microwave pulses, and the respective propagator are given by

$$
H_{\mathrm{free}} = \begin{pmatrix}
\delta_1 & 0 & 0 & 0 \\
0 & 0 & 0 & 0 \\
0 & 0 & \delta_1+\delta_2-g & 0 \\
0 & 0 & 0 & \delta_2
\end{pmatrix}, \qquad U_{\mathrm{free}}(T_f) = \exp(-iH_{\mathrm{free}}T_f) = \begin{pmatrix}
\mathrm{e}^{-\mathrm{i}T_f\delta_1} & 0 & 0 & 0 \\
0 & 1 & 0 & 0 \\
0 & 0 & \mathrm{e}^{\mathrm{i}T_f(-\delta_1-\delta_2+g)} & 0 \\
0 & 0 & 0 & \mathrm{e}^{-\mathrm{i}\delta_2 T_f}
\end{pmatrix}, \tag{D6}
$$

where T_f is the respective free evolution time. We assume that the Rabi frequencies are much stronger than g, δ_1, and δ_2, so we can neglect their effect during the refocusing pulses. Then, the Hamiltonians and propagators of the π pulses on NV1 and NV2 are, respectively,

$$H_{\text{pulse}}^{\text{NV1}} \approx \begin{pmatrix} 0 & \frac{\Omega_1(t)}{2} & 0 & 0 \\ \frac{\Omega_1(t)}{2} & 0 & 0 & 0 \\ 0 & 0 & 0 & \frac{\Omega_1(t)}{2} \\ 0 & 0 & \frac{\Omega_1(t)}{2} & 0 \end{pmatrix}, \quad U_1(\theta_1) = \exp(-iH_{\text{pulse}}^{\text{NV1}} T_1) \approx \begin{pmatrix} \cos(\frac{\theta_1}{2}) & -\mathrm{i}\sin(\frac{\theta_1}{2}) & 0 & 0 \\ -\mathrm{i}\sin(\frac{\theta_1}{2}) & \cos(\frac{\theta_1}{2}) & 0 & 0 \\ 0 & 0 & \cos(\frac{\theta_1}{2}) & -\mathrm{i}\sin(\frac{\theta_1}{2}) \\ 0 & 0 & -\mathrm{i}\sin(\frac{\theta_1}{2}) & \cos(\frac{\theta_1}{2}) \end{pmatrix} \tag{D7}$$

$$H_{\text{pulse}}^{\text{NV2}} \approx \begin{pmatrix} 0 & 0 & \frac{\Omega_2(t)}{2} & 0 \\ 0 & 0 & 0 & \frac{\Omega_2(t)}{2} \\ \frac{\Omega_2(t)}{2} & 0 & 0 & 0 \\ 0 & \frac{\Omega_2(t)}{2} & 0 & 0 \end{pmatrix}, \quad U_2(\theta_2) = \exp(-iH_{\text{pulse}}^{\text{NV2}} T_2) \approx \begin{pmatrix} \cos(\frac{\theta_2}{2}) & 0 & -\mathrm{i}\sin(\frac{\theta_2}{2}) & 0 \\ 0 & \cos(\frac{\theta_2}{2}) & 0 & -\mathrm{i}\sin(\frac{\theta_2}{2}) \\ -\mathrm{i}\sin(\frac{\theta_2}{2}) & 0 & \cos(\frac{\theta_2}{2}) & 0 \\ 0 & -\mathrm{i}\sin(\frac{\theta_2}{2}) & 0 & \cos(\frac{\theta_2}{2}) \end{pmatrix}, \tag{D8}$$

where $\theta_1 = \Omega_1 T_1 = \pi$ and $\theta_2 = \Omega_2 T_2 = \pi$ (we assume that the pulses are rectangular for simplicity of presentation and without loss of generality).

In order to characterize the gate, we consider a sequence of two instantaneous π pulses on each NV and analyze the evolution in the interaction basis of the pulses. The Hamiltonians in each free evolution period are given as follows:

Period 1.—before the first π pulse on NV1:

$$H_{\text{int},1} = H_{\text{free}} = \begin{pmatrix} \delta_1 & 0 & 0 & 0 \\ 0 & 0 & 0 & 0 \\ 0 & 0 & -g+\delta_1+\delta_2 & 0 \\ 0 & 0 & 0 & \delta_2 \end{pmatrix}, \qquad t_1 = \frac{\tau_1}{2}. \tag{D9}$$

Period 2—after one π pulse on NV1, no π pulses on NV2:

$$H_{\text{int},2} = U_{\text{int},2} H_{\text{free}} U_{\text{int},2}^{\dagger} = \begin{pmatrix} 0 & 0 & 0 & 0 \\ 0 & \delta_1 & 0 & 0 \\ 0 & 0 & \delta_2 & 0 \\ 0 & 0 & 0 & -g+\delta_1+\delta_2 \end{pmatrix}, \quad \text{where } U_{\text{int},2} = U_1(\pi), \qquad t_2 = \frac{\tau_1}{2} - \tau_2. \tag{D10}$$

Period 3.—after one π pulse on NV1, one π pulse on NV2:

$$H_{\text{int},3} = U_{\text{int},3} H_{\text{free}} U_{\text{int},3}^{\dagger} = \begin{pmatrix} \delta_2 & 0 & 0 & 0 \\ 0 & -g+\delta_1+\delta_2 & 0 & 0 \\ 0 & 0 & 0 & 0 \\ 0 & 0 & 0 & \delta_1 \end{pmatrix}, \quad \text{where } U_{\text{int},3} = U_2(\pi)U_1(\pi), \qquad t_3 = \frac{\tau_1}{2} + \tau_2. \tag{D11}$$

Period 4.—after two π pulses on NV1, one π pulse on NV2:

$$H_{\text{int},4} = U_{\text{int},4} H_{\text{free}} U_{\text{int},4}^{\dagger} = \begin{pmatrix} -g+\delta_1+\delta_2 & 0 & 0 & 0 \\ 0 & \delta_2 & 0 & 0 \\ 0 & 0 & \delta_1 & 0 \\ 0 & 0 & 0 & 0 \end{pmatrix}, \quad \text{where } U_{\text{int},4} = U_1(\pi)U_2(\pi)U_1(\pi), \quad t_4 = \frac{\tau_1}{2} - \tau_2. \tag{D12}$$

Period 5.—after two π pulses on NV1, two π pulses on NV2:

$$H_{\mathrm{int},5} = U_{\mathrm{int},5} H_{\mathrm{free}} U^{\dagger}_{\mathrm{int},5} = \begin{pmatrix} \delta_1 & 0 & 0 & 0 \\ 0 & 0 & 0 & 0 \\ 0 & 0 & -g+\delta_1+\delta_2 & 0 \\ 0 & 0 & 0 & \delta_2 \end{pmatrix}, \quad \text{where } U_{\mathrm{int},5} = U_2(\pi)U_1(\pi)U_2(\pi)U_1(\pi), \quad t_5 = \tau_2. \tag{D13}$$

The total evolution in the interaction basis is then given by

$$U_{\mathrm{int}} = \exp\left(-i\sum H_{\mathrm{int},k} t_k\right) = \exp(\mathrm{i}\xi_{\mathrm{g}}) \begin{pmatrix} 1 & 0 & 0 & 0 \\ 0 & \mathrm{e}^{\mathrm{i}N_\pi g\tau_2} & 0 & 0 \\ 0 & 0 & \mathrm{e}^{\mathrm{i}N_\pi g\tau_2} & 0 \\ 0 & 0 & 0 & 1 \end{pmatrix}. \tag{D14}$$

where we used $[H_{\mathrm{int},i}, H_{\mathrm{int},j}] = 0$ to obtain the first equality, $\xi_{\mathrm{g}} = N_\pi\{(g/2)[-(\tau_1/2)+\tau_2] + (\tau_1/2)(\delta_1+\delta_2)\}$ is an irrelevant global phase, and N_π is the total number of applied pulses on each NV center, e.g., $N_\pi = 2$, in our example, with two pulses or $N_\pi = 8$ for XY8-1 and $N_\pi = 16$ for XY8-2. Thus, in the following, we define the effective evolution time as $t_{\mathrm{evol}} = N_\pi \tau_2$.

For demonstrating the controlled oscillations of the $\sqrt{ZZ}$ gate with XY8-1 decoupling on the Bloch sphere equator in Fig. 2, we use $\tau_1 = 3000$ ns. This choice allows us to sweep the effective evolution time $t_{\mathrm{evol}} = N_\pi \tau_2$ with a large dynamic range (constrained by $-\tau_1/2 \leq \tau_2 \leq \tau_1/2$), but it is not an optimal choice in terms of fidelity for two reasons.

First, a shorter τ_1 allows us to realize the same gate unitary with shorter total sequence length ($= N_\pi \tau_1$, independent of τ_2) and thus less decoherence. Consequently, for realizing the $\sqrt{ZZ}$ unitary, τ_1 should be chosen close to $\tau_{1,\mathrm{min}} = (2/4N_\pi v_{\mathrm{dip}}) \sim 520$ ns for our $v_{\mathrm{dip}} = 120$ kHz, $N_\pi = 8$ when using XY8-1. We note that using shorter τ_1 for our entangling gate is also possible by increasing N_π in the dynamical decoupling sequence, e.g., using XY8-2, which consists of 16 pulses, as long as $t_{\mathrm{evol}} = N_\pi \tau_2$, with $\tau_2 \leq \tau_1/2$, is kept constant. Decreasing the pulse spacing τ_1 should improve fidelity as the characteristic T_2 time of a decoupling sequence typically increases when the pulse separation is shorter [99–101].

Second, because of the misaligned magnetic field on the target qubit, population transfer to and entanglement with the nitrogen nuclear spin can occur. Since we can choose τ_1 freely (but not τ_2, which is set by ν_{dip}), we use this degree of freedom to minimize such an unwanted interaction with the nitrogen spin. In Fig. 7(a), we probe the polarization loss due to interaction with the nitrogen by initializing the target qubit into superposition and applying a standard XY8-1 experiment only on the target qubit with varying π pulse spacing τ_1. We observe that the simulation well reproduces the experimental data, and we find a $\tau_1 = 800$ ns, which reduces the interaction with the nitrogen spin. In the future, a modified gate microwave sequence could minimize this interaction with the nucleus more strictly [102].

After determining τ_1, our gate calibration for τ_2 is carried out as follows: We initialize the input state $(|0\rangle - i|1\rangle) \otimes (|0\rangle - i|1\rangle)$ and apply the $\sqrt{ZZ}$ gate sequence, with varying τ_2, 4 times ($n = 4$). Repeating the gate improves the accuracy of the calibration, as more oscillation periods are recorded for a τ_2 sweep. To the experimentally recorded

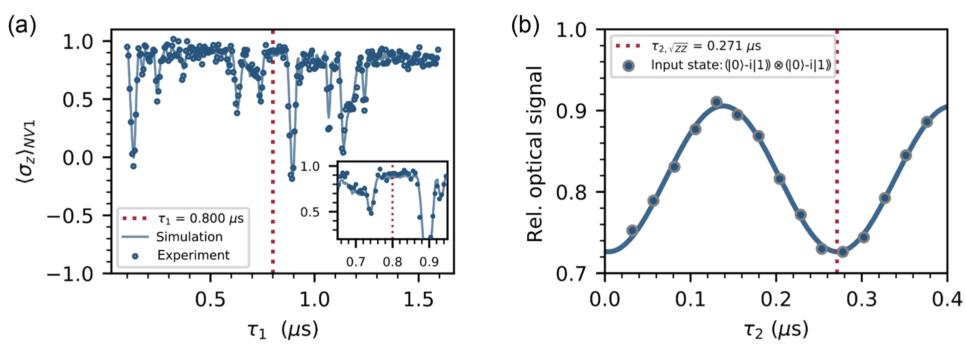

FIG. 7. Entangling gate calibration. (a) XY8-1 experiment performed with pulse spacing τ_1 on the misaligned target NV1 at magnetic field setting 2. (b) Measured repeated application of the $\sqrt{ZZ}$ gate with varying τ_2 [$\tau_1 = 800$ ns, $n_{\mathrm{rep}} = 4$, $\Omega_{\mathrm{Rabi}}/(2\pi) = 22.97$ MHz] for calibration. The projection pulse after the $\sqrt{ZZ}$ gates for both NVs is $\pi_x/2$. The solid line is a fit from which we extract the $\tau_{2,\sqrt{ZZ}}$ that realizes our entangling gate.

oscillation [e.g., in Fig. 7(b)], we fit a sine and find the $\tau_{2,\sqrt{ZZ}}$ that realizes minimal fluorescence, as expected from a quarter rotation (repeated $n = 4$ times) on the Bloch sphere equator.

In order to capture the gate dynamics accurately, we repeat the same calibration procedure to obtain a coupling parameter for our model. In addition to the experiment in Fig. 7(b) at magnetic field setting 2, we also experimentally perform a calibration at magnetic field setting 1 [$\tau_1 = 800$ ns, $n = 4$, $\Omega_{\mathrm{Rabi}}/(2\pi) = 15.51$ MHz, data not shown] and obtain a calibrated $\tau_{2,\sqrt{ZZ},B_1} = 212.6$ ns. We then simulate both calibration experiments individually and find the effective dipolar coupling parameters v_{dip} in Table I that reproduce the experimentally observed $\tau_{2,\sqrt{ZZ},B_1}$, $\tau_{2,\sqrt{ZZ},B_2}$.

The dipole-dipole coupling of 119.8 kHz sets an upper limit of (9.54 ± 0.03) nm on the distance between the NV centers [103]. An exact distance estimate would require knowledge of the relative orientation of the dipoles and could be obtained by repeated DEER measurements in a varying-bias magnetic field [104].

APPENDIX E: CHARGE INITIALIZATION AND READOUT

Our charge initialization is based on a weak orange laser pulse and postselection of the recorded spin readout photons. After the green (552-nm) spin initialization laser pulse, the charge state of a single NV in bulk diamond

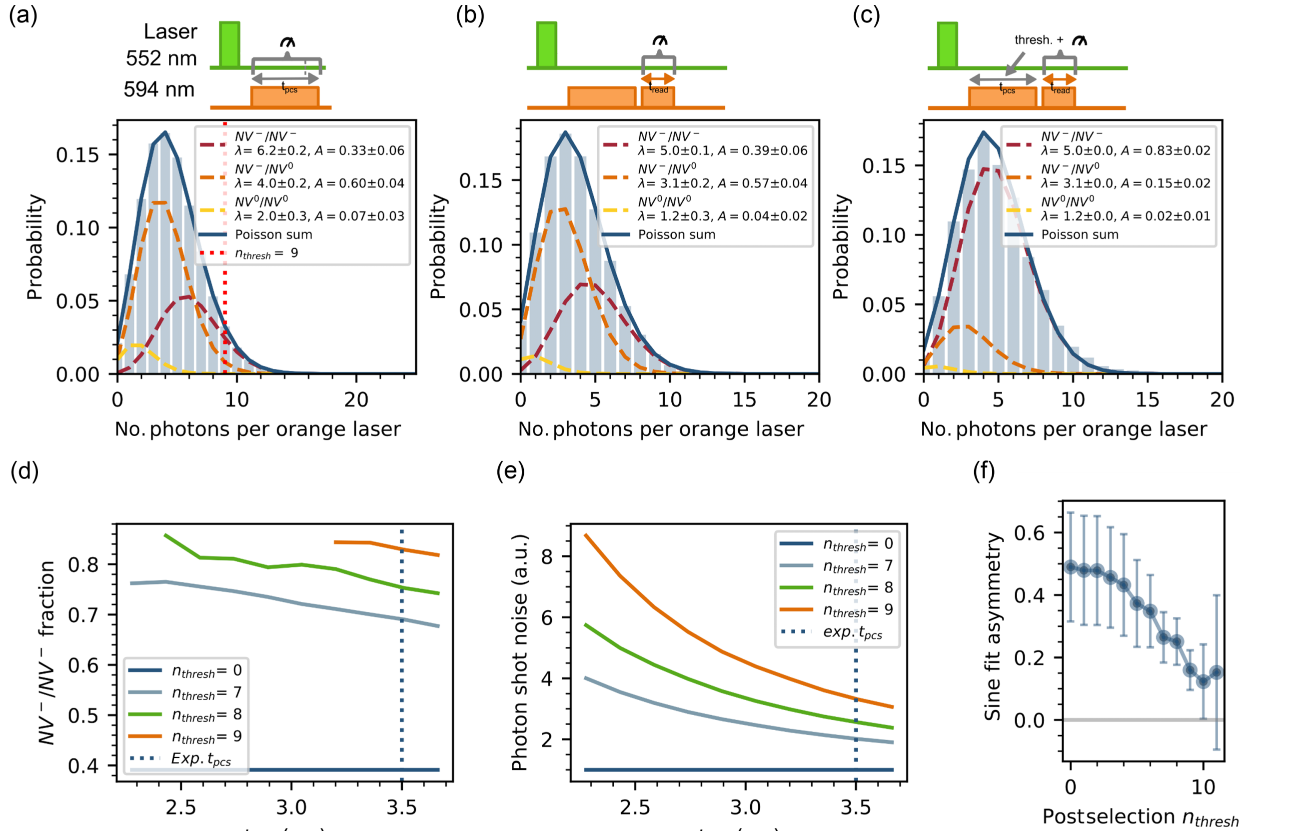

FIG. 8. Charge initialization and readout. (a) Histogram of photons collected during the $t_{\mathrm{pcs}} = 3.5$ ms orange charge initialization pulse. First, the register is initialized with a 3 μs green laser pulse. Dashed lines are the single Poissonian contributions with fitted mean rates λ_i and weight A_i. The chosen thresholding photon number $n_{\mathrm{thresh}} = 9$ used for charge initialization is shown as a red dotted line. (b) Photon histogram collected during the 2.9-ms charge readout laser pulse after the charge initialization laser. (c) Photon histogram with the same data as panel (b) but after applying postselection to analyze only charge readout data if more than $n_{\mathrm{thresh}} = 9$ photons are detected during the charge initialization pulse. The rates λ_i are fixed during fitting to the values extracted in panel (b). We conservatively estimate the error on the charge-state fidelity by giving the uncertainty of the weight parameter A_{--} in panel (b). (d) NV^-/NV^- charge initialization fidelity measured for different lengths t_{pcs} of the gating window, which counts photons during the charge initialization laser [same dataset as in panels (b) and (c)]. A shorter t_{pcs} shifts the Poissonian in the histogram to the left and thus increases charge-state fidelity. Unstable fits are discarded. (e) Photon shot noise as calculated from the number of analyzed photons $(1/\sqrt{n_{\mathrm{phots}}})$ and normalized to the noise without postselection. Increasing the charge-state fidelity comes at the cost of higher readout noise. (f) Asymmetry of the σ_y component of the DEER oscillation presented in Fig. 2(e) while varying the postselection threshold parameter n_{thresh}.

reaches a steady-state occupation of typically $A(\mathrm{NV}^-)/(A(\mathrm{NV}^0)+A(\mathrm{NV}^-)) \sim 0.7$ [38], where A denotes the probability of finding the NV in a certain charge state. The orange laser probes the NV^- absorption with minimal overlap to the NV^0 absorption spectrum. At the same time, its weak power avoids ionization. Thus, more readout photons are expected during the orange laser pulse if both of the NVs are in the negative charge state. In Fig. 8(a), we measure readout photons per 3.5-ms-long orange laser on our coupled NV quantum register after spin initialization with a 3 μs green laser. Because of the limited collection efficiency, the three expected Poissonian peaks $\{(\mathrm{NV}^0,\mathrm{NV}^0);(\mathrm{NV}^0,\mathrm{NV}^-);(\mathrm{NV}^-,\mathrm{NV}^-)\}$ overlap in the histogram. For determination of the charge state, we fit a Poissonian model to the photon probability $p(n_{\mathrm{phot}})$ with free weighting parameters A_i and fitted mean rates λ_i:

$$p(n_{\mathrm{phot}}) = A_{--}P(\lambda_{--}) + A_{-0}P(\lambda_{-0}) + A_{00}P(\lambda_{00}). \tag{E1}$$

The extracted weights of the charge state slightly differ from the values $A_{00}=0.09$, $A_{-0}=0.42$, and $A_{--}=0.49$ expected for an independent combination of two bulk NVs. We speculate that a single charge shared between both NVs is more favorable in our system.

In Fig. 8(b), we append another 2.9-ms-long orange laser pulse to independently probe the charge-state fidelity after the $t_{\mathrm{pcs}}=3.5$ ms-long charge initialization laser pulse, without applying postselection yet. As expected, we recover charge-state weights that are in agreement with the data in Fig. 8(a).

We then continue in Fig. 8(c) to analyze only charge readout data for experimental shots where the counted photons during the first initialization orange laser pulse satisfy a threshold photon $n_{\mathrm{phot}} > n_{\mathrm{thresh}}$. After applying postselection with the experimental settings ($t_{\mathrm{pcs}}=3.5$ ms, $n_{\mathrm{thresh}}=9$) presented in Figs. 2 and 3, we measure an increase in $(\mathrm{NV}^-,\mathrm{NV}^-)$ charge-state initialization fidelity from $(39\pm6)\%$ (no postselection) to $(83\pm6)\%$.

In Figs. 8(d) and 8(e), we characterize the trade-off between higher charge-state fidelity and readout noise: Improved charge initialization can be reached for shorter t_{pcs} or higher n_{thresh}, but as more photons are discarded by the thresholding, the photon shot noise of the readout estimated from the total number of detected photons n_{phots} as $\mathrm{SNR}_{\mathrm{shot}}^{-1} = 1/\sqrt{n_{\mathrm{phots}}}$ increases.

We tune the charge state by varying n_{thresh} in Fig. 8(f). Here, we utilize the σ_y component of the DEER oscillation as an alternative probe of the charge state and observe that its asymmetry reduces to (0.12 ± 0.12) when increasing to $n_{\mathrm{thresh}}=10$, indicating a clearly improved charge-state initialization.

APPENDIX F: SPAM AND ENTANGLING GATE FIDELITY IN A MAGNETIC FIELD

Misaligning the magnetic field against the NV axis in the diamond lattice lowers the spin initialization fidelity by green laser excitation and yields a partly mixed spin state. This effect originates from the altered effective decay rates into the new magnetic ground-state levels that are superpositions of the aligned spin ground states [105]. Here, we estimate the SPAM error given in the main text caused by a reduced spin initialization.

In our (misaligned) magnetic field setting 2, a reduced readout contrast is observed for the misaligned NV1 in Fig. 9(a). We avoid the influence of different orientations of both NVs' optical dipoles by determining the maximum readout contrast for varying orientation of the linearly polarized green (552-nm) excitation laser by a $\lambda/2$ wave plate.

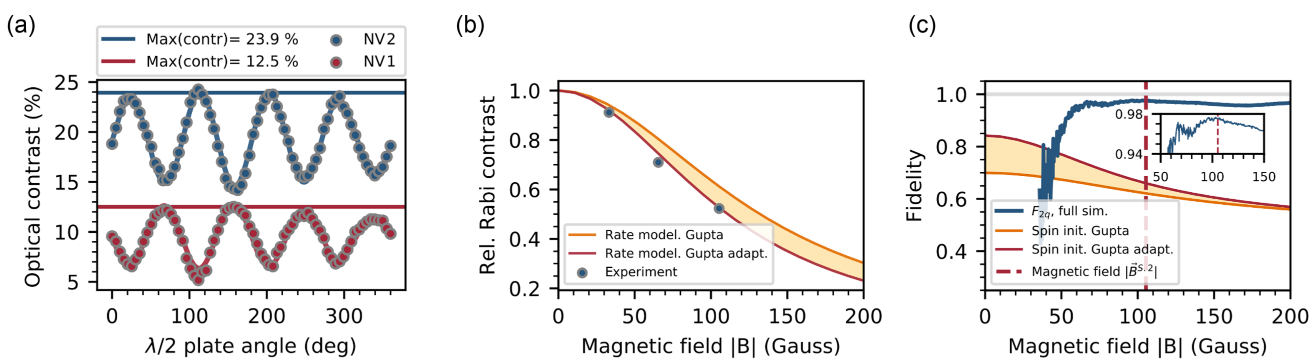

FIG. 9. SPAM error by spin mixing. (a) Optical contrast as measured from fits to Rabi oscillations on both NVs at different $\lambda/2$ wave-plate angles with magnetic field setting 2. The maximum optical contrasts of both NVs is determined from the maximum value of a fitted empirical model (sum of two sines). (b) Relative Rabi contrast $\max(\mathrm{contr}_{\mathrm{NV1}})/\max(\mathrm{contr}_{\mathrm{NV2}})$ at different absolute values of the magnetic field and misalignment angles $\theta_{\mathrm{NV1}} \sim 74°$, with experimental precision $\pm2°$. The solid line is a simulation based on the rate model and transition rates in Table II. Circles are measurement data taken at different magnetic fields as described in panel (a). (c) Simulated $\sqrt{ZZ}$ gate fidelity and spin initialization fidelity for different absolute values of the magnetic field and misalignment angles $\theta_{\mathrm{NV1}} = 74.08°$ and $\theta_{\mathrm{NV2}} = 3.58°$.

In Fig. 9(b), we verify that transformation of a seven-level rate equation model [105] agrees reasonably well with the experimentally observed, relative Rabi contrast $\max(\mathrm{contr}_{\mathrm{NV1}})/\max(\mathrm{contr}_{\mathrm{NV2}})$ at different absolute magnetic field values. The misalignment angle $\theta \approx 74°$ of each data point is similar to in magnetic field setting 2, up to a precision of $\pm 2°$.

We analyze the model with two sets of rates (see Table II):

(1) Optical rates as given in Ref. [106]. To calibrate the laser pump rate as the only free parameter, we minimize the difference from the experimental data. Comparing to our experimental data, we observe a deviation from the model.

(2) Since the intersystem crossing rates are not straightforward to determine, we additionally adapt the rates from the ^{3}E level to the singlet and minimize the difference from experimental data in parallel to the laser pump rate. The resulting rates are better fits to our experimental data.

The same model allows us to estimate the SPAM error introduced by a reduced spin polarization. The electron spin initialization fidelity F_{init} is given by

$$F_{\mathrm{init}} = \frac{p_0}{p_0 + p_{-1} + p_{+1}}. \tag{F1}$$

Note that the experimentally observed readout contrast at the misaligned magnetic field in Figs. 9(a) and 9(b) includes contributions from both the reduced spin polarization and the less-efficient optical readout. To obtain the spin initialization fidelity, we determine the populations p_{m_s} of the $m_s = 0, \pm 1$ levels after a 3-μs green laser and a waiting time of 1 μs.

In Fig. 9(c), we plot the simulated spin initialization fidelity from Eq. (F1) and the entangling gate fidelity [predicted like in Fig. 4(e)] for a varying magnetic field. At zero field (equivalent to no misalignment), the predicted spin initialization fidelity (defined in the spin-1 manifold, mean of both set of rates) is 77%. This value is lower than in experimental work ($\geq 92\%$ [107], $(88 \pm 4)\%$ [103]), indicating that the available models might underestimate the absolute degree of spin polarization.

We estimate the SPAM error due to spin mixing to 17% by dividing the simulated value (mean of both sets of rates) at our magnetic field setting 2 by the value at zero field:

$$\mathrm{err}_{\mathrm{SPAM,init}} = \frac{1 - F_{\mathrm{init}}(B)}{1 - F_{\mathrm{init}}(B = 0)} \tag{F2}$$

For small NV quantum registers, such a SPAM error by spin mixing seems acceptable, especially when a higher gate fidelity can be reached in turn. On the other hand, larger-scale quantum processors will require one to mitigate state mixing, as state preparation errors are only inefficiently correctable [108].

TABLE II. Rates used for modeling (as in Ref. [105]) the readout contrast and spin initialization fidelity in a misaligned magnetic field.

Rates	Model Gupta [106], NV1	Model Gupta, adapted ISC
k_{57}	92.9 MHz	**90.307 MHz**
k_{67}	92.9 MHz	**90.307 MHz**
k_{47}	11.2 MHz	**3.004 MHz**
k_{71}	4.9 MHz	4.9 MHz
k_{72}	2.03 MHz	2.03 MHz
k_{73}	2.03 MHz	2.03 MHz
k_{41}	66.08 MHz	66.08 MHz
k_{52}	66.08 MHz	66.08 MHz
k_{63}	66.08 MHz	66.08 MHz
Laser pump β	1.215	1.938

We observe a trade-off between higher gate fidelity and lower spin initialization fidelity when increasing the magnetic field. Depending on the application, diamond quantum registers with NVs of different orientations may be optimized towards higher entangling gate fidelity or reduced SPAM spin initialization errors.

APPENDIX G: SIMULATED GATE FIDELITIES

In the main text, we discuss the error sources determining the gate set fidelity. In Fig. 10(a), these errors are illustrated in the level structure of the coupled NV system. After spin initialization, both NVs are polarized into the $m_s = 0$ sublevels. Because of the unpolarized nuclear ^{14}N spins at ambient conditions, the initialized state is a mixed state with nearly equal classical probability of the nitrogen populations. However, our quantum register is not formed from the ^{14}N levels, and initially, the electron states are pure (after taking the partial trace).

After and during preparation of arbitrary register input states, multiple gate errors occur:

(i) As the inherent ^{14}N spins of both NVs are unpolarized, the nuclear spin state is random at the beginning of every experimental shot. Consequently, most of the microwave pulses suffer from a detuning $\Delta = \pm A_{ZZ}/(2\pi) = \pm 2.16$ MHz from the correct microwave transition frequency for the electron, if the nitrogen state is $m_I = \pm 1$. This detuning leads to imperfect driving of the three hyperfine lines, as indicated by the orange sketch of the pulse spectrum. Additionally, the unpolarized nitrogen spin causes free evolution on the nonaddressed NV in our single-qubit-gate implementation (that we discuss in Appendix C).

(ii) In a magnetic field setting that is aligned with the NV quantization axis, the diagonal hyperfine interaction tensor $\underline{A} = \sum_{i=x,y,z} A_{ii} S_i \otimes I_i$ in the Hamiltonian (see Sec. IV, Appendix B) effectively only contains $S_z \otimes I_z$ terms. Here, S_i, I_j denote the

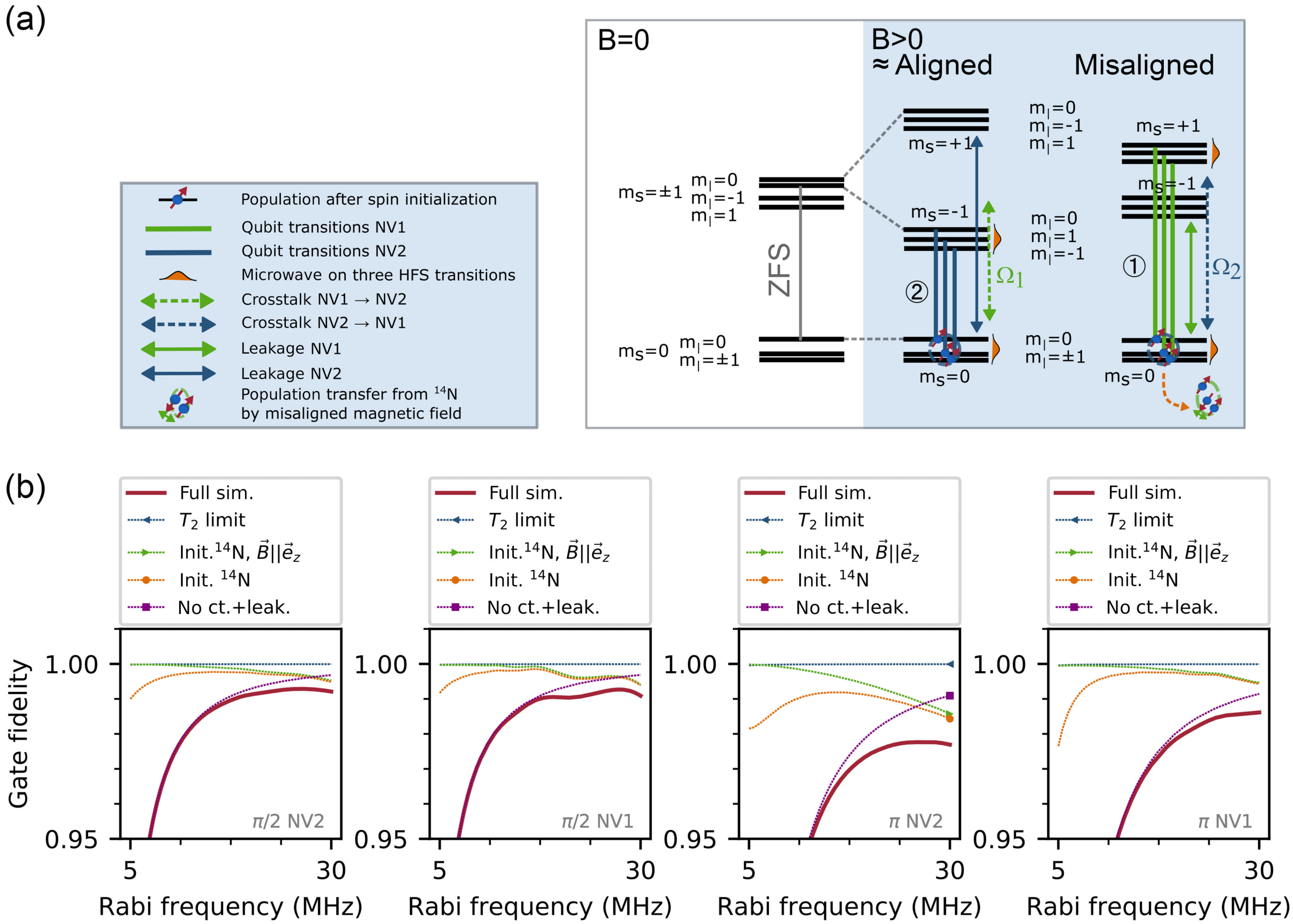

FIG. 10. Gate errors. (a) Level scheme of the $^3A_2$ level of two NVs, including Zeeman and ^{14}N hyperfine interactions. The error sources discussed in the main text are sketched. After spin initialization by the green laser, we obtain pure electron states indicated by blue dashed circles after tracing out the ^{14}N nuclear spins. During a gate, interaction with the thermal nitrogen spin causes depolarization of the electron spin (green dashed ellipse). (b) Simulated gate fidelities for all single-qubit gates (of phase X) of the gate set for different Rabi frequencies. Decoherence is considered as the T_2 process, as described in Sec. IV, and it is much smaller for the shorter single-qubit gates.

$S = I = 1$ spin operator of the NV and ^{14}N spins, respectively. In our geometry, however, magnetic field misalignment is unavoidable, and in the tilted basis, the hyperfine tensor is no longer diagonal. Then, terms of, e.g., the form $S_z \otimes I_x$ appear and can cause entanglement with the nitrogen spin or population transfer from the qubit to the nitrogen spin. Especially during gate operations that contain dynamical decoupling pulses, this result decreases the electron spin polarization (see Appendix F).

(iii) All microwave pulses (driving $m_s = 0, -1$ on NV2, and $m_s = 0, 1$ on NV1) generate a small, unwanted microwave drive on the other NV ["crosstalk," dashed arrows in Fig. 10(a)] or transitions to states out of the qubit subspaces ("leakage," solid arrows).

Note that all error sources may change populations as well as cause unwanted phase shifts.

In Fig. 4(e), we predict the entangling gate fidelity of only the $\sqrt{ZZ}$ gate from our model. We use the same simulation to give gate fidelities for the single-qubit gates of the gate set in Fig. 10(b). As the single-qubit pulses in our experiment do not employ dynamical decoupling, the fidelity improvement expected from polarized ^{14}N nitrogen spins is more pronounced. At high-enough Rabi frequencies, we expect nearly no further improvement by aligning the magnetic field. Consequently, we anticipate that polarizing the nitrogen spins and mitigating crosstalk and leakage by optimal control could enable very-high-quality single-qubit control in multi-NV diamond quantum registers.

APPENDIX H: EXTENDED COHERENCE LIMITS

Using Eq. (5) with coherence times for different decoupling sequences, we estimate the coherence-limited

TABLE III. T_2 coherence times in various experimental scenarios. Assuming the coherent error sources discussed in the context of Fig. 4 are mitigated, the listed decoherence-limited entangling gate fidelities are achievable. For the extended coherence times, the same gate duration t_{gate} as in the current experiment is assumed.

Scenario	Relevant coherence time	t_{gate}	Decoherence-limited gate fidelity $F_{2q,T2}$
Previous best, room temperature, Hahn echo [24]	$\mathrm{avg}(T_{2,\mathrm{HE}}) = 332\ \mu\mathrm{s}$	25.4 μs	0.926
Current experiment, room temperature, Hahn echo	$\mathrm{avg}(T_{2,\mathrm{HE}}) = 103\ \mu\mathrm{s}$	6.4 μs	0.939
Current experiment, room temperature, XY8	$\mathrm{avg}(T_{2,\mathrm{XY8}}) = 465\ \mu\mathrm{s}$	6.4 μs	0.986
Advanced DD, room temperature	$\mathrm{avg}(T_{2,\mathrm{aDD}}) = 2$ ms	6.4 μs [a]	0.996
Carr-Purcell, cryogenic experiment (4 K)	$\mathrm{avg}(T_{2,\mathrm{CP}}) = 1.58$ s [30]	6.4 μs [a]	0.999996

[a]The duration t_{gate} of our two-qubit gate depends on the effective coupling, and it considers the optimized $\tau_1 = 800$ ns.

entangling gate fidelity in realistic experimental scenarios, also cited in Sec. IV F, in Table III.

Specifically, we note that decoherence in NV centers and other color centers in diamond can usually be modeled with an Ornstein-Uhlenbeck process [85,109,110], and one can estimate the expected memory time limit with ideal, instantaneous π pulses for particular pulse spacing τ_1 by [110]

$$T_2(\tau_1) = \left(\frac{T_{2,\mathrm{HE}}}{\tau_1}\right)^2 T_{2,\mathrm{HE}}, \tag{H1}$$

not taking T_1 decay into account. This approach results in much higher theoretical values $T_{2,\mathrm{XY8}}$ of the order of several ms for the particular $\tau_1 = 800$ ns, which is then limited by T_1 relaxation. The lower actual $T_{2,\mathrm{XY8}}$ in our experiment suggests that pulse errors might have an effect on the achieved decoherence times, so using robust dynamical decoupling sequences, e.g., KDD4 or the UR family [100,111], is likely to improve T_2. The improvement itself can be characterized in terms of the transition probability error ϵ of a single π pulse, so the fidelity of a single XY8 sequence is [110]

$$F_{\mathrm{XY8}} \approx 1 - O(\epsilon^3). \tag{H2}$$

In comparison, the fidelities of KDD4 (KDD sequence, nested in the XY4 sequence) [111] and the UR sequences are [100,111]

$$F_{\mathrm{KDD4}} \approx 1 - O(\epsilon^5), \tag{H3}$$

$$F_{\mathrm{URn}} \approx 1 - O(\epsilon^{n/2}). \tag{H4}$$

Thus, using these advanced robust sequences could, in principle, allow us to improve our coherence times towards the $2T_1$ limit, which should be of the order of milliseconds. Following the fidelity estimation in Eq. (5), the decoherence limit of XY8 can be estimated to $F_{2q,\mathrm{XY8}} = 1 - \mathrm{pEPG}_{T2} \approx 0.986$, with the decoherence time for our experiment. Improving the coherence time towards the milliseconds regime would, in principle, push the expected fidelity towards higher values, e.g., $F_{2q,\mathrm{adv}} \approx \exp(-t_{\mathrm{gate}}/T_{2,\mathrm{adv}}) \approx 0.996$ for $T_{2,\mathrm{adv}} \approx 2$ ms with advanced dynamical decoupling sequences. We note that the assumption of simple exponential decay is conservative, as the actual decay rate for dynamical decoupling with an Ornstein-Uhlenbeck noise model is typically a stretched exponential [109,110], which would result in even higher fidelities on the timescale of the gate.

Another approach for extending the coherence limit is operating at low temperatures, which can be beneficial in several aspects. First, T_1 relaxation due to two-phonon Raman and Orbach-type processes is negligible at temperatures of the order of 4 K, boosting T_1 to the order of one hour [30]. This finding results in several orders of improvement in the achievable coherence times, e.g., $T_{2,\mathrm{CP},4\mathrm{K}} \approx 1.58$ s [30], which would, in principle, make the effect of decoherence negligible on the timescales of realistic NV-NV dipolar coupling, yielding $1 - F_{2q,T2,4\mathrm{K}} \approx 4 \times 10^{-6}$. Apart from negligible decoherence, operating at low temperatures, in principle, would allow for the polarization of the nitrogen nuclear spin, reducing the need for high Rabi frequency to cover all hyperfine transitions. Operating with lower Rabi frequencies will, in turn, reduce the effect of crosstalk and leakage, minimizing the detrimental effect of both of these errors, as reported in Fig. 4(d) in the main text.

To compare our gate design with previous work, we also list the decoherence limits of a two-qubit gate under Hahn echo decoupling for both experiments in Table III. Because of its Hahn echolike structure, $T_{2,\mathrm{HE}}$ is the relevant coherence time for the gate in Ref. [24]. We observe a slight improvement in the decoherence-limited gate fidelity for our sample, with an improvement factor of $(1 - F^{[24]}_{2q,T2,\mathrm{HE}})/(1 - F_{2q,T2,\mathrm{HE}}) = 1.21$. While the dipolar coupling is higher for our sample, the coherence time $\mathrm{avg}(T_{2,\mathrm{HE}})$ is shorter, and the ratio $t_{\mathrm{gate}}/\mathrm{avg}(T_2)$ ultimately determines the fidelity limit. Our gate employs higher-order decoupling, thereby extending the limiting coherence timescale to the much longer $T_{2,\mathrm{XY8}}$. Thus, our final infidelity is a factor of $(1 - F_{2q,T2,\mathrm{HE}})/(1 - F_{2q}) = 1.53$ better than our sample's apparent $T_{2,\mathrm{HE}}$ limit. By the increased coherence time, we access a new regime, where the error sources discussed in the main text become relevant.

DATA AVAILABILITY

Some of the data that support the findings of this article are openly available [86]. Datasets are not publicly available. The data are available from the authors upon reasonable request.

[1] F. Arute, K. Arya, R. Babbush, D. Bacon, J. C. Bardin *et al.*, *Quantum supremacy using a programmable superconducting processor*, Nature (London) **574**, 505 (2019).

[2] Sen H. Zhong, H. Wang, Y. H. Deng, M. C. Chen, L. C. Peng *et al.*, *Quantum computational advantage using photons*, Science **370**, 1460 (2020).

[3] Y. Kim, A. Eddins, S. Anand, K. X. Wei, E. van den Berg, S. Rosenblatt, H. Nayfeh, Y. Wu, M. Zaletel, K. Temme, and A. Kandala, *Evidence for the utility of quantum computing before fault tolerance*, Nature (London) **618**, 500 (2023).

[4] D. Bluvstein, S. J. Evered, A. A. Geim, S. H. Li, H. Zhou *et al.*, *Logical quantum processor based on reconfigurable atom arrays*, Nature (London) **626**, 58 (2023).

[5] C. D. Bruzewicz, J. Chiaverini, R. McConnell, and J. M. Sage, *Trapped-ion quantum computing: Progress and challenges*, Appl. Phys. Rev. **6**, 021314 (2019).

[6] K. N. Smith, G. S. Ravi, J. M. Baker, and F. T. Chong, *Scaling superconducting quantum computers with chiplet architectures*, *Proceedings of the Annual International Symposium on Microarchitecture : MICRO 2022* (2022) p. 1092, 10.1109/MICRO56248.2022.00078.

[7] K. Wintersperger, F. Dommert, T. Ehmer, A. Hoursanov, J. Klepsch, W. Mauerer, G. Reuber, T. Strohm, M. Yin, and S. Luber, *Neutral atom quantum computing hardware: Performance and end-user perspective*, Eur. Phys. J. Quantum Technol. **10**, 32 (2023).

[8] J. Wang, F. Sciarrino, A. Laing, and M. G. Thompson, *Integrated photonic quantum technologies*, Nat. Photonics **14**, 273 (2020).

[9] G. Waldherr, Y. Wang, S. Zaiser, M. Jamali, T. Schulte-Herbrüggen, H. Abe, T. Ohshima, J. Isoya, J. F. Du, P. Neumann, and J. Wrachtrup, *Quantum error correction in a solid-state hybrid spin register*, Nature (London) **506**, 204 (2014).

[10] J. Kelly, R. Barends, A. G. Fowler, A. Megrant, E. Jeffrey *et al.*, *State preservation by repetitive error detection in a superconducting quantum circuit*, Nature (London) **519**, 66 (2015).

[11] Z. Chen, K. J. Satzinger, J. Atalaya, A. N. Korotkov, A. Dunsworth *et al.*, *Exponential suppression of bit or phase errors with cyclic error correction*, Nature (London) **595**, 383 (2021).

[12] M. H. Abobeih, Y. Wang, J. Randall, S. J. H. Loenen, C. E. Bradley, M. Markham, D. J. Twitchen, B. M. Terhal, and T. H. Taminiau, *Fault-tolerant operation of a logical qubit in a diamond quantum processor*, Nature (London) **606**, 884 (2022).

[13] B. Foxen, C. Neill, A. Dunsworth, P. Roushan, B. Chiaro *et al.*., *Demonstrating a continuous set of two-qubit gates for near-term quantum algorithms*, Phys. Rev. Lett. **125**, 120504 (2020).

[14] C. J. Ballance, T. P. Harty, N. M. Linke, M. A. Sepiol, and D. M. Lucas, *High-fidelity quantum logic gates using trapped-ion hyperfine qubits*, Phys. Rev. Lett. **117**, 060504 (2016).

[15] H. P. Bartling, J. Yun, K. N. Schymik, M. van Riggelen, L. A. Enthoven, H. B. van Ommen, M. Babaie, F. Sebastiano, M. Markham, D. J. Twitchen, and T. H. Taminiau, *Universal high-fidelity quantum gates for spin-qubits in diamond*, Phys. Rev. Appl. **23**, 034052 (2025).

[16] C. E. Bradley, J. Randall, M. H. Abobeih, R. C. Berrevoets, M. J. Degen, M. A. Bakker, M. Markham, D. J. Twitchen, and T. H. Taminiau, *A ten-qubit solid-state spin register with quantum memory up to one minute*, Phys. Rev. X **9**, 031045 (2019).

[17] G. L. van de Stolpe, D. P. Kwiatkowski, C. E. Bradley, J. Randall, M. H. Abobeih, S. A. Breitweiser, L. C. Bassett, M. Markham, D. J. Twitchen, and T. H. Taminiau, *Mapping a 50-spin-qubit network through correlated sensing*, Nat. Commun. **15**, 1 (2024).

[18] S. Simmons, *Scalable fault-tolerant quantum technologies with silicon color centers*, PRX Quantum **5**, 010102 (2024).

[19] M. Pompili, S. L. N. Hermans, S. Baier, H. K. C. Beukers, P. C. Humphreys, R. N. Schouten, R. F. L. Vermeulen, M. J. Tiggelman, L. dos Santos Martins, B. Dirkse, S. Wehner, and R. Hanson, *Realization of a multinode quantum network of remote solid-state qubits*, Science **372**, 259 (2021).

[20] C. M. Knaut, A. Suleymanzade, Y. C. Wei, D. R. Assumpcao, P. J. Stas, Y. Q. Huan, B. Machielse, E. N. Knall, M. Sutula, G. Baranes, N. Sinclair, C. De-Eknamkul, D. S. Levonian, M. K. Bhaskar, H. Park, M. Lončar, and M. D. Lukin, *Entanglement of nanophotonic quantum memory nodes in a telecom network*, Nature (London) **629**, 573 (2024).

[21] F. Dolde, I. Jakobi, B. Naydenov, N. Zhao, S. Pezzagna, C. Trautmann, J. Meijer, P. Neumann, F. Jelezko, and J. Wrachtrup, *Room-temperature entanglement between single defect spins in diamond*, Nat. Phys. **9**, 139 (2013).

[22] M. J. Degen, S. J. H. Loenen, H. P. Bartling, C. E. Bradley, A. L. Meinsma, M. Markham, D. J. Twitchen, and T. H. Taminiau, *Entanglement of dark electron-nuclear spin defects in diamond*, Nat. Commun. **12**, 3470 (2021).

[23] A. Ungar, P. Cappellaro, A. Cooper, and W. K. C. Sun, *Control of an environmental spin defect beyond the coherence limit of a central spin*, PRX Quantum **5**, 010321 (2024).

[24] F. Dolde, V. Bergholm, Y. Wang, I. Jakobi, B. Naydenov, S. Pezzagna, J. Meijer, F. Jelezko, P. Neumann, T. Schulte-Herbrüggen, J. Biamonte, and J. Wrachtrup, *High-fidelity spin entanglement using optimal control*, Nat. Commun. **5**, 3371 (2014).

[25] J. Kelly, R. Barends, B. Campbell, Y. Chen, Z. Chen *et al.*, *Optimal quantum control using randomized benchmarking*, Phys. Rev. Lett. **112**, 240504 (2014).

[26] P. J. Vetter, T. Reisser, M. G. Hirsch, T. Calarco, F. Motzoi, F. Jelezko, and M. M. Müller, *Gate-set evaluation metrics*

for closed-loop optimal control on nitrogen-vacancy center ensembles in diamond, npj Quantum Inf. **10**, 96 (2024).

[27] I. I. Boradjiev and N. V. Vitanov, *Control of qubits by shaped pulses of finite duration*, Phys. Rev. A **88**, 013402 (2013).

[28] I. S. Mihov and N. V. Vitanov, *Qubit dynamics driven by smooth pulses of finite duration*, Phys. Rev. A **110**, 052609 (2024).

[29] J. Preskill, *Quantum computing in the NISQ era and beyond*, Quantum **2**, 1 (2018).

[30] M. H. Abobeih, J. Cramer, M. A. Bakker, N. Kalb, M. Markham, D. J. Twitchen, and T. H. Taminiau, *One-second coherence for a single electron spin coupled to a multi-qubit nuclear-spin environment*, Nat. Commun. **9**, 2552 (2018).

[31] M. Haruyama, S. Onoda, T. Higuchi, W. Kada, A. Chiba, Y. Hirano, T. Teraji, R. Igarashi, S. Kawai, H. Kawarada, Y. Ishii, R. Fukuda, T. Tanii, J. Isoya, T. Ohshima, and O. Hanaizumi, *Triple nitrogen-vacancy centre fabrication by $C_5N_4H_n$ ion implantation*, Nat. Commun. **10**, 2664 (2019).

[32] G. Waldherr, P. Neumann, S. F. Huelga, F. Jelezko, and J. Wrachtrup, *Violation of a temporal Bell inequality for single spins in a diamond defect center*, Phys. Rev. Lett. **107**, 090401 (2011).

[33] B. Grotz, J. Beck, P. Neumann, B. Naydenov, R. Reuter, F. Reinhard, F. Jelezko, J. Wrachtrup, D. Schweinfurth, B. Sarkar, and P. Hemmer, *Sensing external spins with nitrogen-vacancy diamond*, New J. Phys. **13**, 055004 (2011).

[34] A. M. Souza, G. A. Alvarez, and D. Suter, *Experimental protection of quantum gates against decoherence and control errors*, Phys. Rev. A **86**, 050301(R) (2012).

[35] M. Nielsen and I. Chuang, *Quantum Computation and Quantum Information* (Cambridge University Press, Cambridge, England, 2010).

[36] F. Shi, Q. Zhang, P. Wang, H. Sun, J. Wang, X. Rong, M. Chen, C. Ju, F. Reinhard, H. Chen, J. Wrachtrup, J. Wang, and J. Du, *Single-protein spin resonance spectroscopy under ambient conditions*, Science **347**, 1135 (2015).

[37] Y. X. Liu, A. Ajoy, and P. Cappellaro, *Nanoscale vector dc magnetometry via ancilla-assisted frequency up-conversion*, Phys. Rev. Lett. **122**, 100501 (2019).

[38] N. Aslam, G. Waldherr, P. Neumann, F. Jelezko, and J. Wrachtrup, *Photo-induced ionization dynamics of the nitrogen vacancy defect in diamond investigated by single-shot charge state detection*, New J. Phys. **15**, 013064 (2013).

[39] L. Marseglia, J. P. Hadden, A. C. Stanley-Clarke, J. P. Harrison, B. Patton, Y. L. D. Ho, B. Naydenov, F. Jelezko, J. Meijer, P. R. Dolan, J. M. Smith, J. G. Rarity, and J. L. O'Brien, *Nanofabricated solid immersion lenses registered to single emitters in diamond*, Appl. Phys. Lett. **98**, 133107 (2011).

[40] D. Wirtitsch, G. Wachter, S. Reisenbauer, M. Gulka, V. Ivády, F. Jelezko, A. Gali, M. Nesladek, and M. Trupke, *Exploiting ionization dynamics in the nitrogen vacancy center for rapid, high-contrast spin, and charge state initialization*, Phys. Rev. Res. **5**, 013014 (2023).

[41] K. Groot-Berning, N. Raatz, I. Dobrinets, M. Lesik, P. Spinicelli, A. Tallaire, J. Achard, V. Jacques, J. F. Roch, A. M. Zaitsev, J. Meijer, and S. Pezzagna, *Passive charge state control of nitrogen-vacancy centres in diamond using phosphorous and boron doping*, Phys. Status Solidi **211**, 2268 (2014).

[42] J. Geng, T. Shalomayeva, M. Gryzlova, A. Mukherjee, S. Santonocito, D. Dzhavadzade, D. B. R. Dasari, H. Kato, R. Stöhr, A. Denisenko, N. Mizuochi, and J. Wrachtrup, *Dopant-assisted stabilization of negatively charged single nitrogen-vacancy centers in phosphorus-doped diamond at low temperatures*, npj Quantum Inf. **9**, 110 (2023).

[43] Y. Doi, T. Fukui, H. Kato, T. Makino, S. Yamasaki, T. Tashima, H. Morishita, S. Miwa, F. Jelezko, Y. Suzuki, and N. Mizuochi, *Pure negatively charged state of the NV center in n-type diamond*, Phys. Rev. B **93**, 081203(R) (2016).

[44] A. M. Souza, G. A. Álvarez, and D. Suter, *Robust dynamical decoupling*, Phil. Trans. R. Soc. A **370**, 4748 (2012).

[45] P. Coote, R. Dimov, S. Maity, G. S. Hartnett, M. J. Biercuk, and Y. Baum, *Resource-efficient context-aware dynamical decoupling embedding for arbitrary large-scale quantum algorithms*, PRX Quantum **6**, 010332 (2025).

[46] E. Magesan, J. M. Gambetta, and J. Emerson, *Scalable and robust randomized benchmarking of quantum processes*, Phys. Rev. Lett. **106**, 180504 (2011).

[47] J. M. Chow, J. M. Gambetta, A. D. Córcoles, S. T. Merkel, J. A. Smolin, C. Rigetti, S. Poletto, G. A. Keefe, M. B. Rothwell, J. R. Rozen, M. B. Ketchen, and M. Steffen, *Universal quantum gate set approaching fault-tolerant thresholds with superconducting qubits*, Phys. Rev. Lett. **109**, 060501 (2012).

[48] S. F. Huelga, C. Macchiavello, T. Pellizzari, A. K. Ekert, M. B. Plenio, and J. I. Cirac, *Improvement of frequency standards with quantum entanglement*, Phys. Rev. Lett. **79**, 3865 (1997).

[49] J.-S. Chen, E. Nielsen, M. Ebert, V. Inlek, K. Wright, V. Chaplin, A. Maksymov, E. Páez, A. Poudel, P. Maunz, and J. Gamble, *Benchmarking a trapped-ion quantum computer with 29 algorithmic qubits*, Quantum **8**, 1516 (2024).

[50] S. J. Evered, D. Bluvstein, M. Kalinowski, S. Ebadi, T. Manovitz, H. Zhou, S. H. Li, A. A. Geim, T. T. Wang, N. Maskara, H. Levine, G. Semeghini, M. Greiner, V. Vuletić, and M. D. Lukin, *High-fidelity parallel entangling gates on a neutral-atom quantum computer*, Nature (London) **622**, 268 (2023).

[51] F. Marxer, A. Vepsäläinen, S. W. Jolin, J. Tuorila, A. Landra *et al.*, *Long-distance transmon coupler with CZ-gate fidelity above 99.8%*, PRX Quantum, **4**, 010314 (2023).

[52] B. Smeltzer, J. McIntyre, and L. Childress, *Robust control of individual nuclear spins in diamond*, Phys. Rev. A **80**, 050302(R) (2009).

[53] M. Chen, M. Hirose, and P. Cappellaro, *Measurement of transverse hyperfine interaction by forbidden transitions*, Phys. Rev. B **92**, 020101(R) (2015).

[54] E. Tiesinga, P. J. Mohr, D. B. Newell, and B. N. Taylor, *Codata recommended values of the fundamental physical constants: 2018*, Rev. Mod. Phys. **93**, 025010 (2021).

[55] A. Antušek, K. Jackowski, M. Jaszuński, W. Makulski, and M. Wilczek, *Nuclear magnetic dipole moments from NMR spectra*, Chem. Phys. Lett. **411**, 111 (2005).

[56] F. Motzoi, J. M. Gambetta, P. Rebentrost, and F. K. Wilhelm, *Simple pulses for elimination of leakage in weakly nonlinear qubits*, Phys. Rev. Lett. **103**, 1 (2009).

[57] M. M. Müller, R. S. Said, F. Jelezko, T. Calarco, and S. Montangero, *One decade of quantum optimal control in the chopped random basis*, Rep. Prog. Phys. **85**, 076001 (2022).

[58] Z. Kazi, I. M. Shelby, H. Watanabe, K. M. Itoh, V. Shutthanandan, P. A. Wiggins, and K. M. C. Fu, *Wide-field dynamic magnetic microscopy using double-double quantum driving of a diamond defect ensemble*, Phys. Rev. Appl. **15**, 1 (2021).

[59] D. S. Wang, A. G. Fowler, and L. C. L. Hollenberg, *Surface code quantum computing with error rates over 1 percent*, Phys. Rev. A **83**, 020302(R) (2011).

[60] A. G. Fowler, M. Mariantoni, J. M. Martinis, and A. N. Cleland, *Surface codes: Towards practical large-scale quantum computation*, Phys. Rev. A **86**, 032324 (2012).

[61] I. Schwartz, J. Scheuer, B. Tratzmiller, S. Müller, Q. Chen, I. Dhand, Z. Y. Wang, C. Müller, B. Naydenov, F. Jelezko, and M. B. Plenio, *Robust optical polarization of nuclear spin baths using Hamiltonian engineering of nitrogen-vacancy center quantum dynamics*, Sci. Adv. **4**, 1 (2018).

[62] J. Scheuer, I. Schwartz, S. Müller, Q. Chen, I. Dhand, M. B. Plenio, B. Naydenov, and F. Jelezko, *Robust techniques for polarization and detection of nuclear spin ensembles*, Phys. Rev. B **96**, 174436 (2017).

[63] V. Jacques, P. Neumann, J. Beck, M. Markham, D. Twitchen, J. Meijer, F. Kaiser, G. Balasubramanian, F. Jelezko, and J. Wrachtrup, *Dynamic polarization of single nuclear spins by optical pumping of nitrogen-vacancy color centers in diamond at room temperature*, Phys. Rev. Lett. **102**, 057403 (2009).

[64] T. Chakraborty, J. Zhang, and D. Suter, *Optimization of a quantum control sequence for initializing a nitrogen-vacancy spin register*, Phys. Rev. A **105**, 022622 (2022).

[65] S. Bodenstedt, I. Jakobi, J. Michl, I. Gerhardt, P. Neumann, and J. Wrachtrup, *Nanoscale spin manipulation with pulsed magnetic gradient fields from a hard disc drive writer*, Nano Lett. **18**, 5389 (2018).

[66] H. Zhang, K. Arai, C. Belthangady, J.-C. Jaskula, and R. L. Walsworth, *Selective addressing of solid-state spins at the nanoscale via magnetic resonance frequency encoding*, npj Quantum Inf. **3**, 31 (2017).

[67] M. Werninghaus, D. J. Egger, F. Roy, S. Machnes, F. K. Wilhelm, and S. Filipp, *Leakage reduction in fast superconducting qubit gates via optimal control*, npj Quantum Inf. **7**, 14 (2021).

[68] P. Rembold, N. Oshnik, M. M. Müller, S. Montangero, T. Calarco, and E. Neu, *Introduction to quantum optimal control for quantum sensing with nitrogen-vacancy centers in diamond*, AVS Quantum Sci. **2**, 024701 (2020).

[69] S. J. Glaser, U. Boscain, T. Calarco, C. P. Koch, W. Köckenberger, R. Kosloff, I. Kuprov, B. Luy, S. Schirmer, T. Schulte-Herbrüggen, D. Sugny, and F. K. Wilhelm, *Training Schrödinger's cat: Quantum optimal control: Strategic report on current status, visions and goals for research in Europe*, Eur. Phys. J. D **69**, 279 (2015).

[70] D. M. Irber, F. Poggiali, F. Kong, M. Kieschnick, T. Lühmann, D. Kwiatkowski, J. Meijer, J. Du, F. Shi, and F. Reinhard, *Robust all-optical single-shot readout of nitrogen-vacancy centers in diamond*, Nat. Commun. **12**, 532 (2021).

[71] L. Robledo, L. Childress, H. Bernien, B. Hensen, P. F. A. Alkemade, and R. Hanson, *High-fidelity projective read-out of a solid-state spin quantum register*, Nature (London) **477**, 574 (2011).

[72] W. Pfaff, B. J. Hensen, H. Bernien, S. B. Van Dam, M. S. Blok, T. H. Taminiau, M. J. Tiggelman, R. N. Schouten, M. Markham, D. J. Twitchen, and R. Hanson, *Unconditional quantum teleportation between distant solid-state quantum bits*, Science **345**, 532 (2014).

[73] P. Neumann, J. Beck, M. Steiner, F. Rempp, H. Fedder, P. R. Hemmer, J. Wrachtrup, and F. Jelezko, *Single-shot readout of a single nuclear spin*, Science **329**, 542 (2010).

[74] K. Kimura, S. Onoda, K. Yamada, W. Kada, T. Teraji, J. Isoya, O. Hanaizumi, and T. Ohshima, *Creation of multiple NV centers by phthalocyanine ion implantation*, Appl. Phys. Express **15**, 066501 (2022).

[75] T. Unden, P. Balasubramanian, D. Louzon, Y. Vinkler, M. B. Plenio, M. Markham, D. Twitchen, A. Stacey, I. Lovchinsky, A. O. Sushkov, M. D. Lukin, A. Retzker, B. Naydenov, L. P. McGuinness, and F. Jelezko, *Quantum metrology enhanced by repetitive quantum error correction*, Phys. Rev. Lett. **116**, 1 (2016).

[76] J. Cramer, N. Kalb, M. A. Rol, B. Hensen, M. S. Blok, M. Markham, D. J. Twitchen, R. Hanson, and T. H. Taminiau, *Repeated quantum error correction on a continuously encoded qubit by real-time feedback*, Nat. Commun. **7**, 1 (2016).

[77] Q. Zhang, Y. Guo, W. Ji, M. Wang, J. Yin, F. Kong, Y. Lin, C. Yin, F. Shi, Y. Wang, and J. Du, *High-fidelity single-shot readout of single electron spin in diamond with spin-to-charge conversion*, Nat. Commun. **12**, 1529 (2021).

[78] M. Joliffe, V. Vorobyov, and J. Wrachtrup, *Readout of strongly coupled NV center-pair spin states with deep neural networks*, arXiv1–8 (2024) 10.48550/arXiv.2412.19581.

[79] T. Teraji, T. Yamamoto, K. Watanabe, Y. Koide, J. Isoya, S. Onoda, T. Ohshima, L. J. Rogers, F. Jelezko, P. Neumann, J. Wrachtrup, and S. Koizumi, *Homoepitaxial diamond film growth: High purity, high crystalline quality, isotopic enrichment, and single color center formation*, Phys. Status Solidi **212**, 2365 (2015).

[80] E. L. Hahn, *Spin echoes*, Phys. Rev. **80**, 580 (1950).

[81] D. Suter and F. Jelezko, *Single-spin magnetic resonance in the nitrogen-vacancy center of diamond*, Prog. Nucl. Magn. Reson. Spectrosc. **98–99**, 50 (2017).

[82] J. M. Binder, A. Stark, N. Tomek, J. Scheuer, F. Frank, K. D. Jahnke, C. Müller, S. Schmitt, M. H. Metsch, T. Unden, T. Gehring, A. Huck, U. L. Andersen, L. J. Rogers, and F. Jelezko, *Qudi: A modular python suite for experiment control and data processing*, SoftwareX **6**, 85 (2017).

[83] *Qiskit: An Open-source Framework for Quantum Computing*, 10.5281/zenodo.2573505 (2023).

[84] X. F. He, N. B. Manson, and P. T. H. Fisk, *Paramagnetic resonance of photoexcited N-V defects in diamond. I. Level*

anticrossing in the 3A ground state, Phys. Rev. B **47**, 8809 (1993).

[85] N. Bar-Gill, L. M. Pham, A. Jarmola, D. Budker, and R. L. Walsworth, *Solid-state electronic spin coherence time approaching one second*, Nat. Commun. **4**, 1743 (2013).

[86] G. de Lange, Z. H. Wang, D. Ristè, V. V. Dobrovitski, and R. Hanson, *Universal dynamical decoupling of a single solid-state spin from a spin bath*, Science **330**, 60 (2010).

[87] E. Bauch, S. Singh, J. Lee, C. A. Hart, J. M. Schloss, M. J. Turner, J. F. Barry, L. M. Pham, N. Bar-Gill, S. F. Yelin, and R. L. Walsworth, *Decoherence of ensembles of nitrogen-vacancy centers in diamond*, Phys. Rev. B **102**, 134210 (2020).

[88] T. Proctor, K. Rudinger, K. Young, M. Sarovar, and R. Blume-Kohout, *What randomized benchmarking actually measures*, Phys. Rev. Lett. **119**, 130502 (2017).

[89] C. J. Wood and J. M. Gambetta, *Quantification and characterization of leakage errors*, Phys. Rev. A **97**, 032306 (2018).

[90] T. Joas, Plot data, 10.5281/zenodo.14825963.

[91] G. Balasubramanian, I. Y. Chan, R. Kolesov, M. Al-Hmoud, J. Tisler, C. Shin, C. Kim, A. Wojcik, P. R. Hemmer, A. Krueger, T. Hanke, A. Leitenstorfer, R. Bratschitsch, F. Jelezko, and J. Wrachtrup, *Nanoscale imaging magnetometry with diamond spins under ambient conditions*, Nature (London) **455**, 648 (2008).

[92] F. Dolde, H. Fedder, M. W. Doherty, T. Noebauer, F. Rempp, G. Balasubramanian, T. Wolf, F. Reinhard, L. C. L. Hollenberg, F. Jelezko, J. Wrachtrup, and T. Nöbauer, *Electric-field sensing using single diamond spins*, Nat. Phys. **7**, 459 (2011).

[93] P. Jamonneau, M. Lesik, J. P. Tetienne, I. Alvizu, L. Mayer, A. Dréau, S. Kosen, J. F. Roch, S. Pezzagna, J. Meijer, T. Teraji, Y. Kubo, P. Bertet, J. R. Maze, and V. Jacques, *Competition between electric field and magnetic field noise in the decoherence of a single spin in diamond*, Phys. Rev. B **93**, 024305 (2016).

[94] P. Kehayias, M. J. Turner, R. Trubko, J. M. Schloss, C. A. Hart, M. Wesson, D. R. Glenn, and R. L. Walsworth, *Imaging crystal stress in diamond using ensembles of nitrogen-vacancy centers*, Phys. Rev. B **100**, 174103 (2019).

[95] S. Knauer, J. P. Hadden, and J. G. Rarity, *In-situ measurements of fabrication induced strain in diamond photonic-structures using intrinsic colour centres*, npj Quantum Inf. **6**, 50 (2020).

[96] M. H. Goerz, D. M. Reich, and C. P. Koch, *Optimal control theory for a unitary operation under dissipative evolution*, New J. Phys. **16**, 055012 (2014).

[97] P. J. Vetter, A. Marshall, G. T. Genov, T. F. Weiss, N. Striegler, E. F. Großmann, S. Oviedo-Casado, J. Cerrillo, J. Prior, P. Neumann, and F. Jelezko, *Zero- and low-field sensing with nitrogen-vacancy centers*, Phys. Rev. Appl. **17**, 044028 (2022).

[98] Z. H. Wang, G. De Lange, D. Ristè, R. Hanson, and V. V. Dobrovitski, *Comparison of dynamical decoupling protocols for a nitrogen-vacancy center in diamond*, Phys. Rev. B **85**, 155204 (2012).

[99] C. L. Degen, F. Reinhard, and P. Cappellaro, *Quantum sensing*, Rev. Mod. Phys. **89**, 035002 (2017).

[100] G. T. Genov, D. Schraft, N. V. Vitanov, and T. Halfmann, *Arbitrarily accurate pulse sequences for robust dynamical decoupling*, Phys. Rev. Lett. **118**, 133202 (2017).

[101] D. Suter and G. A. Álvarez, *Colloquium: Protecting quantum information against environmental noise*, Rev. Mod. Phys. **88**, 041001 (2016).

[102] J. Casanova, Z. Y. Wang, J. F. Haase, and M. B. Plenio, *Robust dynamical decoupling sequences for individual-nuclear-spin addressing*, Phys. Rev. A **92**, 042304 (2015).

[103] P. Neumann, R. Kolesov, B. Naydenov, J. Beck, F. Rempp, M. Steiner, V. Jacques, G. Balasubramanian, M. L. Markham, D. J. Twitchen, S. Pezzagna, J. Meijer, J. Twamley, F. Jelezko, and J. Wrachtrup, *Quantum register based on coupled electron spins in a room-temperature solid*, Nat. Phys. **6**, 249 (2010).

[104] D. Yudilevich, R. Stöhr, A. Denisenko, and A. Finkler, *Mapping single electron spins with magnetic tomography*, Phys. Rev. Appl. **18**, 054016 (2022).

[105] J. P. Tetienne, L. Rondin, P. Spinicelli, M. Chipaux, T. Debuisschert, J. F. Roch, and V. Jacques, *Magnetic-field-dependent photodynamics of single NV defects in diamond: An application to qualitative all-optical magnetic imaging*, New J. Phys. **14**, 103033 (2012).

[106] A. Gupta, L. Hacquebard, and L. Childress, *Efficient signal processing for time-resolved fluorescence detection of nitrogen-vacancy spins in diamond*, J. Opt. Soc. Am. B **33**, B28 (2016).

[107] G. Waldherr, J. Beck, M. Steiner, P. Neumann, A. Gali, T. H. Frauenheim, F. Jelezko, and J. Wrachtrup, *Dark states of single nitrogen-vacancy centers in diamond unraveled by single shot NMR*, Phys. Rev. Lett. **106**, 157601 (2011).

[108] M. R. Geller and M. Sun, *Toward efficient correction of multiqubit measurement errors: Pair correlation method*, Quantum Sci. Technol. **6**, 025009 (2021).

[109] D. T. Gillespie, *The mathematics of Brownian motion and Johnson noise*, Am. J. Phys. **64**, 225 (1996).

[110] K. Senkalla, G. Genov, M. H. Metsch, P. Siyushev, and F. Jelezko, *Germanium vacancy in diamond quantum memory exceeding 20 ms*, Phys. Rev. Lett. **132**, 026901 (2024).

[111] A. M. Souza, G. A. Ávarez, and D. Suter, *Robust dynamical decoupling for quantum computing and quantum memory*, Phys. Rev. Lett. **106**, 240501 (2011).